Author/s:
Deore, P;Tsang Min Ching, SJ;Nitschke, MR;Rudd, D;Brumley, DR;Hinde, E;Blackall, LL;van Oppen, MJH

Title:
Unique photosynthetic strategies employed by closely related Breviolum minutum strains under rapid short-term cumulative heat stress

Date:
2024

Citation:
Deore, P., Tsang Min Ching, S. J., Nitschke, M. R., Rudd, D., Brumley, D. R., Hinde, E., Blackall, L. L. & van Oppen, M. J. H. (2024). Unique photosynthetic strategies employed by closely related Breviolum minutum strains under rapid short-term cumulative heat stress. Journal of Experimental Botany, 75 (13), pp.4005-4023. https://doi.org/10.1093/jxb/erae170.

Persistent Link:
https://hdl.handle.net/11343/353920

Journal of Experimental Botany, Vol. 75, No. 13 pp. 4005–4023, 2024
https://doi.org/10.1093/jxb/erae170 Advance Access Publication 18 April 2024

RESEARCH PAPER

Unique photosynthetic strategies employed by closely related *Breviolum minutum* strains under rapid short-term cumulative heat stress

Pranali Deore[1,*], Sarah Jane Tsang Min Ching[1], Matthew R. Nitschke[2,3], David Rudd[4], Douglas R. Brumley[5], Elizabeth Hinde[6], Linda L. Blackall[1], and Madeleine J. H. van Oppen[1,2]

[1] School of BioSciences, The University of Melbourne, Parkville 3010, Victoria, Australia
[2] Australian Institute of Marine Science, Townsville 4810, Queensland, Australia
[3] School of Biological Sciences, Victoria University of Wellington, Wellington 6102, New Zealand
[4] Drug Delivery, Disposition and Dynamics, Monash Institute of Pharmaceutical Sciences, Monash University, Parkville, VIC 3052, Australia
[5] School of Mathematics and Statistics, The University of Melbourne, Parkville 3010, Victoria, Australia
[6] School of Physics, The University of Melbourne, Parkville 3010, Victoria, Australia

* Correspondence: pranali.deore@unimelb.edu.au

Received 20 November 2023; Editorial decision 10 April 2024; Accepted 17 April 2024

Editor: Elizabete Carmo-Silva, Lancaster University, UK

Abstract

The thermal tolerance of symbiodiniacean photo-endosymbionts largely underpins the thermal bleaching resilience of their cnidarian hosts such as corals and the coral model *Exaiptasia diaphana*. While variation in thermal tolerance between species is well documented, variation between conspecific strains is understudied. We compared the thermal tolerance of three closely related strains of *Breviolum minutum* represented by two internal transcribed spacer region 2 profiles (one strain B1–B1o–B1g–B1p and the other two strains B1–B1a–B1b–B1g) and differences in photochemical and non-photochemical quenching, de-epoxidation state of photopigments, and accumulation of reactive oxygen species under rapid short-term cumulative temperature stress (26–40 °C). We found that *B. minutum* strains employ distinct photoprotective strategies, resulting in different upper thermal tolerances. We provide evidence for previously unknown interdependencies between thermal tolerance traits and photoprotective mechanisms that include a delicate balancing of excitation energy and its dissipation through fast relaxing and state transition components of non-photochemical quenching. The more thermally tolerant *B. minutum* strain (B1–B1o–B1g–B1p) exhibited an enhanced de-epoxidation that is strongly linked to the thylakoid membrane melting point and possibly membrane rigidification minimizing oxidative damage. This study provides an in-depth understanding of photoprotective mechanisms underpinning thermal tolerance in closely related strains of *B. minutum*.

Abbreviations: α, light harvesting efficiency; Ddx, diadinoxanthin; $\delta F/F_m'$, effective maximum photosynthetic yield of photosystem II; DES, de-epoxidation state (ratio of Dtx to Ddx); DPI, diphenyleneiodonium; DTT, dithiothreitol; Dtx, diatoxanthin; E_k, minimum saturation irradiance; F_m, maximal fluorescence; F_m', light adapted maximal fluorescence; F_o, minimum fluorescence; F_v/F_m, maximum photosynthetic yield of photosystem II; ITS2, internal transcribed spacer region 2; LHCII, light harvesting complex II; NPQ, non-photochemical quenching; NPQ_{SV}, NPQ determined using the Stern–Volmer equation; PSI, photosystem I; PSII, photosystem II; qE, fast relaxing NPQ; qI, slow relaxing NPQ; qL, coefficient of photochemical quenching; qN, coefficient of non-photochemical quenching; qT_1, state transition 1→2; qT_2, state transition 2→1; ROS, reactive oxygen species; Y(NO), quantum yield of non-regulated energy dissipation; Y(NPQ), quantum yield of regulated energy dissipation.

Keywords: Climate change, intra-specific variation, non-photochemical quenching, photoprotection, Symbiodiniaceae, thermal tolerance.

Introduction

Symbiodiniaceae are microalgal intracellular symbionts of a range of cnidarian hosts such as corals and sea anemones (Nitschke *et al.*, 2022), providing photosynthetically fixed carbon in return for nitrogen from their host (Dubinsky and Jokiel, 1994). Stress tolerance levels of these algae are central to the survival of their hosts (Rowan and Knowlton, 1995; Berkelmans and van Oppen, 2006), especially during summer heatwaves (Baum *et al.*, 2023) that often drive dysbiosis between Symbiodiniaceae and coral hosts causing bleaching (Hoegh-Guldberg, 1999). For instance, species in the genus *Durusdinium* generally confer higher bleaching tolerance to their hosts compared with their *Cladocopium* counterparts (Berkelmans and van Oppen, 2006; Cunning *et al.*, 2015; Silverstein *et al.*, 2015), and the presence of different members of the *Cladocopium* C15 radiation correlates with differential thermal tolerance of corals (Hoadley *et al.*, 2021; Starko *et al.*, 2023). Thermal tolerance in Symbiodiniaceae revolves around their ability to maintain a high maximum photosynthetic yield (F_v/F_m) of photosystem II (PSII) (Dilernia *et al.*, 2023) and high levels of carbon fixation under heat stress (Buerger *et al.*, 2020).

Variation in thermal tolerance in Symbiodiniaceae is reported to be genus- (Baker, 2004), species- (Díaz-Almeyda *et al.*, 2011) and occasionally strain-specific (Howells *et al.*, 2012; Díaz-Almeyda *et al.*, 2017; Russnak *et al.*, 2021). Further, inter-strain variation in other functional and physiological responses has also been reported. For example, cultured *Breviolum antillogorgium* and *Breviolum minutum* showed strain-specific variation in chlorophyll content, photosynthetic efficiency, growth rate (Bayliss *et al.*, 2019), and relative cell size (Aihara *et al.*, 2016) under elevated light and temperature conditions.

In the sea anemone *Exaiptasia diaphana* from the Great Barrier Reef, Dungan *et al.* (2020, 2022) reported the presence of four distinct internal transcribed spacer region 2 (ITS2) profiles, B1–B1o–B1p, B1–B1a–B1b, B1–B1a–B14a–B1n, and B1–B1a–B1b–B1g, of *Breviolum minutum*, each considered to represent a different strain. One of these strains, B1–B1o–B1p, is hypothesized to confer enhanced bleaching tolerance to the host under elevated light (Dungan *et al.*, 2020) and temperature (Dungan *et al.*, 2022). However, an understanding of the mechanisms underpinning the variation in thermal tolerance among the strains is lacking.

Breviolum minutum is predominantly observed in endosymbiosis with cnidarian hosts in the Caribbean and the Atlantic, and is less abundant in the Pacific and Indo-Pacific (van Oppen *et al.*, 2009). Thermal tolerance in cultured *B. minutum* is mainly attributed to a high thylakoid melting point (Díaz-Almeyda *et al.*, 2011; Mansour *et al.*, 2018) and activation of cyclic electron transport (Dang *et al.*, 2019). The thylakoid melting point is the temperature at which PSII (which is composed of proteins and pigments) embedded within the thylakoid membrane of chloroplast is partly (~50%) functional (Mansour *et al.*, 2018). Under elevated temperature, the thylakoid membrane integrity is compromised, resulting in increased production of oxygen radicals. These reactive oxygen species (ROS) leak into the cytoplasm (Tchernov *et al.*, 2004) where they cause cellular oxidative damage and lipid peroxidation (Weis, 2008). Excess production of ROS is caused by the re-routing of the electron flow (Mehler-like reaction) to oxygen as an electron acceptor, resulting in singlet oxygen species production (Roberty *et al.*, 2014), which activates ROS scavenging pathways (Neubauer and Yamamoto, 1994; Asada, 2019). Alternatively, the excess electron flow manifests as activation of cyclic electron transport, whereby electrons are re-routed around components of photosystem I (PSI), which under ambient conditions is a linear process (from PSII to PSI) (Dang *et al.*, 2019). This essentially balances the excitation pressure exerted on PSII (leading to inactivity) (Slavov *et al.*, 2016) while generating a pH gradient across the thylakoid membrane, which is required for ATP synthesis (Johnson *et al.*, 2014). The presence of cyclic electron transport under elevated temperature conditions in *B. minutum* has previously been reported by Dang *et al.* (2019). Unperturbed electron transport through linear (Zaks *et al.*, 2012) or cyclic pathways (Aihara *et al.*, 2016) collectively contributes to photochemical quenching of photo-energy, but upon saturation leads to activation of numerous photoprotective pathways for safe dissipation of excess energy, such as non-photochemical quenching (Goss and Lepetit, 2015).

Currently, the precise mechanistic process of the photoprotective response and its relevance to thermotolerance in strains of *B. minutum* are unknown. This study examines inter-strain variation in thermal tolerance as observed *in hospite* by Dungan *et al.* (2020, 2022). We monitored several photophysiological traits such as ROS formation, de-epoxidation state (DES) of photopigments (diadinoxanthin, Ddx; and diatoxanthin, Dtx), and different components of photochemical and non-photochemical quenching (NPQ) under rapid short-term cumulative heat stress (26–40 °C). Our results show how differences in these photophysiological traits may govern the divergent thermal tolerances in cultured strains of *B. minutum*.

Materials and methods

Isolation of *Breviolum minutum* from the sea anemone *Exaiptasia diaphana*

The genotypes of *Exaiptasia diaphana* used in this study were AIMS2 and AIMS3 (Dungan *et al.*, 2020). *Exaiptasia diaphana* samples were obtained

from the National Sea Simulator (SeaSim) at the Australian Institute of Marine Science (AIMS), which contains materials from the Great Barrier Reef; thus, the anemones are of Great Barrier Reef origin although the exact source location is unknown. The animals were maintained in the Marine Microbial Symbiont Facility (MMSF) at the University of Melbourne in 4 litre polycarbonate tanks holding artificial sea water prepared by reconstituting Red Sea Salt™ in reverse osmosis water to achieve 34‰ salinity. The tanks were unaerated and incubated at 26 °C and 12–15 μmol m^{-2} s^{-1} light intensity (white light emitting diodes, LEDs) under a 12:12 h light–dark cycle. The low light levels were used as the Great Barrier Reef anemones are highly light-sensitive. The anemones were fed freshly hatched *Artemia salina* (brine shrimp, Salt Creek, UT, USA) nauplii twice a week. Tanks were cleaned 2 h post-feeding to remove uneaten material and algal debris using disposable plastic pipettes, followed by replenishment with fresh artificial sea water.

Breviolum minutum cultures were isolated from the two genotypes of *E. diaphana* according to the protocol of Tortorelli *et al.* (2020). *Exaiptasia diaphana* (n=5 animals per genotype) were harvested from tanks and gently washed twice using 5 ml filtered (0.22 μm membrane) Red Sea Salt™ solution and a disposable plastic pipette. Specimens were added to an autoclave-sterilized homogenizer (2 ml Dounce glass tissue grinder) with 1 ml of Diago's IMK medium (Novachem, cat. no. 398-01333). Anemone tissues were crushed for ~5 min or until a homogeneous suspension was obtained. The tissue homogenate was centrifuged at 3000×g for 5 min and the pellet was washed thrice with IMK. Finally, the tissue pellet was suspended in 200 μl of IMK, half of which was snap-frozen in liquid nitrogen and stored at −20 °C for 18S rRNA gene metabarcoding analysis. The remaining 100 μl was plated (20 μl per plate) along with sterile glass beads (ColiRollers, Novagen; cat. no. 71013-3) onto IMK agar (1%) plates supplemented with ampicillin (100 μg ml^{-1}), gentamicin (100 μg ml^{-1}), and nystatin (5 μg ml^{-1}). Colonies that grew after 20 d incubation were selected and re-streaked onto fresh IMK agar plates four times in intervals of 21 d to obtain monoclonal cultures. Plates were incubated at 26 °C and 30–35 μmol m^{-2} s^{-1} light intensity (LEDs) under a 12:12 h light–dark cycle. Single colonies were inoculated to 0.5 ml of liquid IMK and the culture volume was raised up to 20 ml in the same medium over a period of 2 weeks. The final cell concentration was 1×10^6 cells ml^{-1} (Countess II FL automated cell counter, Thermo Fisher Scientific) for molecular biological, cell morphological, and photophysiological analyses as outlined below.

A monoclonal culture of *B. minutum* (SCF-127-01 isolated from the Great Barrier Reef *E. diaphana*) was obtained from AIMS in 2017 and subsequently maintained in the MMSF in IMK at 26 °C and 30–35 μmol m^{-2} s^{-1} light intensity (LEDs) under a 12:12 h light–dark cycle.

For cell size estimations, bright-field images of three strains of *B. minutum* (n=55, 49, and 66 for SCF-127, A2-6, and A3-S12, respectively) were acquired using a ×60 oil immersion objective (numerical aperture 1.4, Nikon Eclipse Ti2-E microscope) and an autoexposure setting within NIS-Elements software (AR 5.30.02). The greyscale microscopy images were converted to 8-bit and threshold range of 90–120 was applied to eliminate any background and retain only cells for further analysis (Fiji 2.9.0, National Institutes of Health, USA). The diameter of the cells was determined using Analyze Particles option wherein the cells within size and circularity ranges of 3 μm to infinity and 0.4–1, respectively, were considered for analysis.

Genetic characterization of strains using ITS2 metabarcoding

DNA was extracted from *E. diaphana* (n=5) tissue homogenates and monoclonal cultures of *B. minutum* (SCF-127 and two monoclonal cultures obtained from *E. diaphana* genotypes AIMS2 and AIMS3) using the extraction protocol described by Wilson *et al.* (2002). Briefly, 0.375 ml of freshly prepared filtered (0.22 μm pore size membrane) extraction buffer (Tris buffer pH 9, 100 mM EDTA, 100 mM NaCl, 1% SDS, 0.2 mg ml^{-1} lysozyme) was added to the homogenate followed by vortexing and incubation at 37 °C for 30 min. Extraction buffer alone served as an extraction blank. Proteinase K (Promega, USA) at a final concentration of 0.5 mg ml^{-1} was added to degrade protein. Samples were subjected to physical cell lysis using ~100 mg sterile glass beads (425–600 μm) followed by bead beating for 30 s at 30 Hz (Qiagen TissueLyser II). Samples were then incubated at 65 °C for 60 min. DNA was precipitated by adding 0.45 mM of ice-cold potassium acetate followed by 30 min of incubation on ice. Samples were centrifuged twice at 15 000×g for 5 min, and the supernatant was harvested and treated with RNAse (final concentration 0.13 mg ml^{-1}, Astral Scientific, Australia) followed by 30 min incubation at 37 °C. DNA was purified and precipitated using 500 μl of ice-cold iso-propanol, and samples were mixed gently and incubated at room temperature for 15 min. DNA was pelleted by centrifuging samples at 15 000×g for 15 min. DNA pellets were washed twice with ice-cold ethanol and centrifuged at 15 000×g for 2 min. All samples were air dried at room temperature for ~40 min and DNA was resuspended in MilliQ water.

Metabarcoding of the ITS2 in DNA of the tissue homogenates (from *E. diaphana* AIMS2 and AIMS3, n=5) and the monoclonal *B. minutum* cultures (three cultures) was performed (Hume *et al.*, 2019) as follows. DNA samples were amplified using Sym_Var_5.8S2 5′-GTGACCTATGAACTCAGGAGTCGAATTGCAGAACTCCGTGAACC-3′ (Hume *et al.*, 2015) and Sym_Var_Rev 5′-CTGAGACTTGCACATCGCAGCCGGGTTCWCTTGTYTGACTTCATGC-3′ (Hume *et al.*, 2013) primers (Sigma-Aldrich, Australia) which had Illumina adapters attached (underlined regions). The PCR mixtures contained 1× MyTaq Hot start Red mix (Bioline, USA), 0.2 μM of forward and reverse primers, and 4 μl of DNA to a final volume of 55 μl by adding DNase free water (Thermo Fisher Scientific). Aliquots of 15 μl were added to three separate 96-well microtitre plates as replicates. These plates were subjected to one cycle of initial denaturation at 95 °C for 3 min; 18 cycles of denaturation at 95 °C for 15 s, annealing at 55 °C for 30s, and extension at 72 °C for 30 s; followed by a final extension at 72 °C for 7 min. The amplicons from three technical replicates of each sample were subsequently pooled for metabarcoding library preparation. The remaining 10 μl of PCR mixtures were subjected to 35 cycles of PCR using conditions outlined above to inspect the PCR amplicons by agarose gel electrophoresis. Each 96-well microtitre plate contained at least three extraction blanks and no DNA template controls to check for potential DNA contaminants present in chemicals used for nucleic acid extraction and PCR mix, respectively. Of the 45 μl of pooled PCR products, 20 μl was aliquoted and mixed with 20 μl of sterile NGS beads (NucleoMag, Macherey-Nagel, Germany) and briefly centrifuged for 5–10 s. Reaction mixtures were incubated at room temperature for 5 min to enable binding of DNA to the beads. The beads were pulled to one side by placing 96-well microtitre plate on a magnetic rack (Thermo Fisher Scientific) and the leftover reaction mix was gently removed by pipetting. The beads were washed twice with 150 μl of 70% v/v ethanol. Plates were air dried for ~10 min to evaporate ethanol, and 40 μl of DNase free water was added to elute DNA from the beads. Plates were placed onto the magnetic rack to enable separation of the liquid containing DNA from the magnetic beads. Cleaned DNA (10 μl) was transferred to a new 96-well microtitre plate and mixed with forward and reverse indexing primers at a final concentration of 0.25 μM along with 1× master mix (MyTaq Hot start Red). The PCR conditions were initial denaturation at 95 °C for 3 min; 24 cycles of denaturation at 95 °C for 30 s, annealing at 60 °C for 30 s, and extension at 72 °C for 30 s; and final extension at 72 °C for 7 min. Aliquots (3 μl) of all samples were analysed by agarose gel electrophoresis to inspect amplicon sizes and potential non-specific amplification. All samples along with extraction blanks and negative controls (5 μl each) were pooled and mixed with 30 μl of NGS beads in 1.5 ml centrifuge tube (Eppendorf® LoBind) to capture DNA onto the beads. The centrifuge tube was incubated at room temperature on a magnetic rack (3D printed custom made for centrifuge tubes) and DNA-beads were washed twice with 180 μl of 80% v/v ethanol. The remaining ethanol was removed by pipetting, and the

centrifuge tube was air dried prior to DNA elution into 150 µl of DNase free water. Eluted DNA was transferred to a new tube and sequenced at the Walter and Eliza Hall Institute, Australia on an Illumina MiSeq platform using a 2 × 300 bp.

The raw Illumina MiSeq sequence reads from *E. diaphana* tissue homogenates and *B. minutum* monoclonal cultures were submitted to SymPortal (SymPortal.org) for quality control and ITS2 type profiling (Hume *et al.*, 2019). The normalized relative abundance of ITS2 type profiles based on presence or absence of defining intragenomic variants (unique ITS2 sequences) in each sample were obtained from the SymPortal database and plotted in R Studio using the ggplot package.

Rapid short-term cumulative heat stress assay

The thermal melting point of thylakoid membrane for three monoclonal *B. minutum* cultures was determined in a rapid short-term cumulative heat stress (28, 30, 32, 33, 34, 35, 40 °C; refer to Supplementary Fig. S1 for experimental design) assay using a modified protocol of Díaz-Almeyda *et al.* (2011). Briefly, 50 ml of exponential growth phase cultures of *B. minutum* were harvested and centrifuged at 3000×*g* for 5 min. The supernatant was discarded, and the pellet was diluted using sterile IMK to achieve a cell concentration of 3×10^6 cells ml^{-1} (automated counter, Countess II FL automated cell counter, Thermo Fisher Scientific). Triplicate centrifuge tubes containing 1.5 ml of cultures were incrementally exposed to 28–40 °C (see above) for 30 min at each temperature. The thylakoid membrane melting point was determined with an imaging pulse-amplitude modulator (iPAM, Walz, Germany) mounted on top of a heat block (Thermo Scientific) to hold centrifuge tubes and provide temperature control. The maximum quantum yield (F_v/F_m) (Table 1) was recorded for each temperature of exposure (28–40 °C, see above) and 26 °C was treated as the ambient control. The reverse sigmoidal curve using F_v/F_m (maximum quantum yield of PSII) values as a function of each temperature of exposure (28–40 °C, see above) was fitted using Weibull's equation in R studio. The thylakoid membrane melting point was determined using the E_{50} parameter (the temperature at which the maximum photosynthetic yield of PSII has dropped by 50% compared with ambient conditions) extracted from predicated temperature values in curve fitting. At the end of each exposure temperature, 1 ml of the cultures was harvested and centrifuged at 3000×*g* for 5 min. The cell pellets were snap-frozen in liquid nitrogen and stored at −80 °C until pigment extraction.

Chlorophyll *a* fluorescence induction and relaxation kinetics

The chlorophyll *a* fluorescence induction and relaxation kinetics of the cultures (under incremental temperature conditions, 28–40 °C) using iPAM was performed to estimate the photosynthetic parameters outlined in Table 1. The cultures were normalized to 3×10^6 cells ml^{-1} and 1.5 ml aliquots in centrifuge tubes were dark adapted for 10 min. The kinetics settings were pre-optimized to obtain reliable fluorescence signals with minimal noise. The measuring light intensity of 10 µmol m^{-2} s^{-1}, frequency of 2 Hz (gain and damping=2) was applied to record dark adapted minimum fluorescence (F_o) when reaction centres were open. Subsequently, a saturation pulse of 10 000 µmol m^{-2} s^{-1} intensity for 760 ms was applied to induce the closure of reaction centres and the maximal fluorescence (F_m) was recorded. With the delay time of 40 s, samples were exposed to repeated exposure of saturation pulses with 20 s intervals in the presence of actinic light (470 nm) of 81 µmol m^{-2} s^{-1} intensity. The induction kinetics in the presence of actinic light was recorded for 315 s prior to the activation of far-red light (780 nm) for relaxation kinetics. The actinic light was turned off and recovery kinetics were reported for 850 s after the end of induction kinetics. The suitable non-saturating actinic light intensity for each *B. minutum* strain was determined using a rapid light curve performed separately. The in-built FluoroWin software was used for construction of rapid light curve for which fresh 1.5 ml cultures (without dark adaptation and incubated at 26 °C) were exposed to incremental intensities of actinic light (1, 10, 20, 35, 55, 80, 110, 145, 185, 230, 280, 335, 395, 460, 530, 610, 700, 800, 925 µmol m^{-2} s^{-1}), each applied for 20 s. A model described by Eilers and Peeters (1988) was used to fit rapid light curves to determine non-saturating actinic light intensity that was in between half the maximum relative electron transport rate value and photoinhibitory intensities. The components of NPQ under relaxation (dark) conditions were computed using dynamic selection of F_m' as described.

In a separate experiment, cultures were treated with metabolic inhibitors (at 26 °C) such as ammonium chloride (5 mM), dithiothreitol (DTT, 20 mM) and diphenyleneiodonium chloride (DPI, 1 µM) to evaluate abolishment of NPQ (Roháček *et al.*, 2014). The estimation of the photosynthetic parameters' effective quantum yield ($\delta F/F_m'$), Stern–Volmer non-photochemical quenching (NPQ_{SV}), coefficient of photochemical quenching (qL), re-oxidation potential (1−qL), minimum saturation irradiance point (E_k), quantum yield of regulated (YNPQ) and non-regulated (YNO) heat dissipation, and fast (qE type), slow relaxing (qI type), state transition 1→2 (qT_1), and state transition 2→1 (qT_2) components of NPQ were estimated using formulae described in Table 1. Rapid light curve fitting was used for estimation of maximum electron transport rate and light harvesting efficiency (α) parameters (Eilers and Peeters, 1988).

Estimation of reactive oxygen species

One hundred microlitres of culture from each replicate tube was harvested at the end of each incubation period (50 min to mimic same duration as 20 min of induction and relaxation kinetics followed by 30 min of hold at elevated temperature) prior to the next exposure temperature and was mixed with 5 µM of a chloromethyl derivative of 2′,7′-dichlorofluorescin diacetate (CM-H_2DCFDA) dye (Thermo Fisher Scientific). Samples were incubated at 28 °C for 60 min. The resultant fluorescence adducts formed due to oxidation of chloromethyl derivative of 2′-7′-dichlorodihydrofluorescein diacetate (CM-H_2DCFDA) by ROS were measured using a plate reader (CLARIOstar plus microplate reader, BMG Labtech, Ortenberg, Germany) with excitation at 484–493 nm and emission at 517–527 nm. The background fluorescence from dye mixed with medium alone was subtracted from results obtained for each *B. minutum* strain (SCF-127, A2-6, A3-S12) in control conditions and ROS levels were normalized to cell density. The assay was pre-optimized for working dye concentration using diluted hydrogen peroxide (H_2O_2, 0–16 mM) and cell density (2×10^4–1×10^6 cells ml^{-1}) (Supplementary Fig. S2) (Nielsen *et al.*, 2018; Ezequiel *et al.*, 2023).

Pigment extraction and estimation of de-epoxidation state

Pigments were extracted from frozen samples thawed on ice using 1.5 ml ice-cold 95% methanol followed by sonication at 40 Hz for 7 min (Sommella *et al.*, 2018). Samples were centrifuged at 3000×g for 5 min (at 4 °C) and the supernatant was filtered through 0.22 µm membranes to remove debris. The extracts were stored at −80 °C before being subjected to ultra-high performance liquid chromatography (UHPLC; Nexera X2 System, with a diode array detector, SPD-M30A, Shimadzu) for separation of pigments using a modification of a reported method (Sommella *et al.*, 2018). A reverse phase C18 column (InfinityLab Poroshell 120 EC-C18, 2.1 × 50 mm, 2.7 µm, Agilent) was operated using a gradient of solvent A (10 mM ammonium acetate in MilliQ water) and solvent B (60:25:15 v/v/v, acetonitrile:isopropanol:methanol), with a column oven temperature maintained at 40 °C. The starting ratio was set at 60% B for 1 min, followed by a gradient to 100% B for 4 min, 2 min of 100% B, 0.30 min of gradient back to 60% B, followed by 1 min of 60% B at a flow rate of 0.4 ml min^{-1}. The sample injection volume was 6 µl with sampling speed of 5 µl s^{-1} and acquisition scan rate of 12.5 Hz. The pigments were

Table 1. List of photosynthetic parameters estimated based on chlorophyll *a* fluorescence induction and relaxation kinetics, rapid light curve fitting and de-epoxidation state (DES)

Parameters	Formulae	Biological relevance	References
Maximum photosynthetic yield of PSII, F_v/F_m	$\frac{F_m - F_o}{F_m}$	Efficiency of PSII to perform photochemistry	Klughammer and Schreiber (2008)
Effective quantum yield, $\delta F/F_m'$	$\frac{F_m' - F_o'}{F_m'}$	Efficiency of PSII to perform photochemistry in steady state (light)	Klughammer and Schreiber (2008)
Coefficient of photochemical quenching based on puddle model, qP	$\frac{F_m' - F}{F_m' - F_o'}$	Excitation pressure or Q_A redox state	Oxborough and Baker (1997)
Coefficient of photochemical quenching based on lake model, qL	$\mathrm{qP} \times \left(\frac{F_o'}{F}\right)$	Open or close state of the PSII reaction centres; term 1–qL indicate fraction of closed reaction centres	Kramer *et al.* (2004)
Stern–Volmer non-photochemical quenching, NPQ_{SV}	$\frac{F_m}{F_m'} - 1$	Overall dissipation of excess energy as heat	Klughammer and Schreiber (2008)
Electron transport rate, ETR	$\frac{F_v}{F_m} \times 0.84 \times 0.5 \times \mathrm{PAR}$	Rate of electron transport from PSII to PSI	Schreiber (2004)
Coefficient of non-photochemical quenching, qN	$\frac{F_m - F_m'}{F_m - F_o'}$	Contribution of NPQ under steady state actinic illumination	Schreiber and Klughammer (2008)
Quantum yield of regulated energy dissipation, Y(NPQ)	$1 - \frac{(F_m' - F)}{F_m} - \frac{1}{\left(\mathrm{NPQ} + 1 + \mathrm{qL}\left(\frac{F_m}{F_o}\right) - 1\right)}$	Energy dissipation through regulated process such as activation of qE	Kramer *et al.* (2004)
Quantum yield of non-regulated energy dissipation, Y(NO)	$\frac{1}{\mathrm{NPQ} + 1 + \mathrm{qL}\left(\frac{F_m}{F_o} - 1\right)}$	Non-regulated component NPQ mediated by non-radiative decay and fluorescence	(Kramer *et al.*, 2004)
Minimum saturation irradiance, E_k (μmole m^{-2} s^{-1})	$E_k = \frac{\mathrm{ETR}_{max}}{\alpha}$	Point above which NPQ is dominant over photochemical quenching	Ralph and Gademann (2005)
Fast relaxing NPQ, qE type	$\left(\frac{F_m - F_m'5}{F_m'5}\right) - \left(\frac{F_m - \mathrm{max}F_m'6\text{–}20}{\mathrm{max}F_m'6\text{–}20}\right)$	Energy dependent component activated upon build-up of pH gradient across thylakoid membrane and activation of cyclic electron flow	Aihara *et al.* (2016), Herdean *et al.* (2023)
Slow relaxing NPQ, qI type	$\left(\frac{F_m - \mathrm{max}F_m'6\text{–}20}{\mathrm{max}F_m'6\text{–}20}\right)$	Damage to reaction centres of PSII caused by photoinhibition	Herdean *et al.* (2023)
State transition I, qT_1 type	$\left(\frac{F_m\mathrm{in\ light} - \mathrm{max}F_m'6\text{–}20}{\mathrm{max}F_m'6\text{–}20}\right) - \left(\frac{F_m\mathrm{in\ dark} - \mathrm{max}F_m'6\text{–}20}{\mathrm{max}F_m'6\text{–}20}\right)$	LHCII are associated with PSII	Herdean *et al.* (2023)
State transition II, qT_2 type	$\left(\frac{F_m - \mathrm{max}F_m'6\text{–}20}{\mathrm{max}F_m'6\text{–}20}\right) - \left(\frac{F_m - \mathrm{min}F_m'6\text{–}20}{\mathrm{min}F_m'6\text{–}20}\right)$	LHCII detach and re-organize with PSI	Herdean *et al.* (2023)
De-epoxidation state, DES	$\mathrm{Dtx}/(\mathrm{Ddx} + \mathrm{Dtx})$	Essential for activation of qE type NPQ component; maintenance of membrane fluidity and Dtx incorporated in thylakoid membrane acts as an antioxidant	Lepetit *et al.* (2010), Bojko *et al.* (2019)

All parameters are dimensionless unless indicated otherwise. α, light harvesting efficiency, a fit parameter estimated by fitting of rapid light curve; Ddx, diadinoxanthin; Dtx, diatoxanthin; ETR_{max}, electron transport maximum; F_o, dark adapted minimal fluorescence; F_m, dark adapted maximal fluorescence; F_m', maximum fluorescence in presence of actinic light; $F_m'5$, maximum fluorescence after 5 min of actinic light exposure; maxF_m'6–20, maximum fluorescence after 5 min of actinic illumination, i.e. during dark relaxation; PAR, photosynthetically active radiation (μmol m^{-2} s^{-1}).

profiled across the UV-visible range between 190 and 800 nm. Pigment peaks were identified using extracted ion chromatograms at 256, 430, and 664 nm, based on the absorption maxima and secondary peaks in each UV profile. Pure chlorophylls *a* and *b* (Sigma-Aldrich) in methanol were used as reference standards for calibration and retention time matching. Further confirmation of pigments was conducted using a parallel LC-MS

analysis (Shimadzu-8030 LC-MS/MS) based on the same chromatographic conditions used for quantitative profiling. Peaks corresponding to peaks detected using UHPLC-UV (with matching retention time) were scanned in both positive and negative ionization mode, using a Q1 scan method across the range of 220–1200 m/z at a scan rate of 15 000 mass units s^{-1}. The DES (Table 1) was determined based on the relative abundance of diadinoxanthin (Ddx, abs max: 448 nm and 478) and diatoxanthin (Dtx, abs max: 442 nm and 472 nm) peaks that were successively detected (Venn *et al.*, 2006) with a characteristic retention time of 4.5 and 4.6 min, respectively (Supplementary Fig. S3) in this study.

Statistical data analysis

All univariate statistical analyses to estimate interaction effects between the three *B. minutum* strains (SCF-127, A2-6, A3-S12) and temperatures were performed using two-way ANOVA (repeated measures) and post-hoc Tukey's multiple comparison test in GraphPad Prism 9.5.0 software (GraphPad Software, USA). A post-hoc analysis, Dunnett's multiple comparison test, was used to evaluate the impact of increasing temperatures (28–40 °C) for each *B. minutum* strain compared with the ambient condition. The level of significance for all the analyses was $P<0.05$. A multivariate principal component analysis (PCA) was performed where all photosynthetic parameters and temperature were dependent and independent variables, respectively. PCA with maximal co-variance used prcomp from the stats packages in R Studio (4.3.1) and the ggplot package was used for visualization of PCA bi-plots. The numerical data used for analysis are available at Figshare repository, doi: 10.6084/m9.figshare.25511563.v1.

Results

Breviolum minutum: ITS2 profiles, cell sizes, and thylakoid membrane thermal melting points

The ITS2 metabarcoding yielded a total of 798 826 raw reads (minimum: 2957; mean: 51 411; maximum: 90 555) across *in hospite* communities of *E. diaphana* (n=5 for each of AIMS2 and AIMS3) and three monoclonal cultures of *B. minutum* strains (n=3 per strain). A total of 364 785 reads (minimum: 280; mean: 20 689; maximum: 44 924) remained post-quality-control. The *in hospite* Symbiodiniaceae from *E. diaphana* were predominantly characterized as B1–B1a–B1b–B1g (80%), whereas the B1–B1o–B1g–B1p (20%) ITS2 profile was present in only one clonal anemone from each *E. diaphana* genotype (Fig. 1A). *Breviolum minutum* SCF-127 had the B1–B1o–B1g–B1p ITS2 profile. Strains A2-6 and A3-S12 were also identified as *B. minutum*, and had an identical ITS2 profile (B1–B1a–B1b–B1g) that is distinct from SCF-127 (Fig. 1B). Our three algal strains are 100% identical to *B. minutum* strain RT02 (CCMP2460) isolated from *E. pallida* (Lajeunesse *et al.*, 2012) on the basis of mitochondrial cytochrome *b* gene (*cob*) sequence comparison (NCBI accession JX213579.1 and JX213581.1). The mean cell diameter of SCF-127 (n=55 cells), A2-6 (n=49 cells) and A3-S12 (n=60 cells) was 8.23 ± 0.7, 7.93 ± 0.8, and 8.46 ± 0.7 µm, respectively. Only strain A3-S12 was significantly larger (6.2%, unpaired *t*-test, P=0.0011) compared with other strains (Fig. 1C). The thylakoid membrane thermal melting point for SCF-127 (35.37 ± 0.02 °C, $P<0.0001$) was significantly higher than for A2-6 (33.99 ± 0.1 °C) and A3-S12 (34.02 ± 0.1 °C) (Fig. 2; Supplementary Fig. S4).

Photophysiological responses under temperature stress

A principal component analysis (Fig. 3A) indicated that all three *B. minutum* strains showed a clear stress response at the highest temperature (40 °C) as determined by alteration of Y(NPQ), Stern–Volmer NPQ (NPQ_{SV}), and qN. At the ambient temperature of 26 °C, the minimum (F_o) and maximum (F_m) levels were marginally higher in A2-6 and A3-S12 compared with SCF-127 (Supplementary Fig. S4A, B). This parameter (F_o) declined marginally in A2-6 and A3-S12 with increasing temperatures. No significant differences among the strains were observed for F_m (Supplementary Fig. S5B; Supplementary Table S1). At 26 °C, SCF-127 showed significantly elevated levels of $\delta F/F_m'$ ($P<0.0001$) compared with the other strains (Fig. 3B). The level of 1−qL showed marginal differences among all strains, although this parameter in combination with $\delta F/F_m'$ contributed to photophysiological performance of SCF-127 (Fig. 3A–C). Under increasing temperature conditions, both $\delta F/F_m'$ and 1−qL showed contrasting trends (Fig. 3B and C, respectively). The F_v/F_m parameter, which is a widely used indicator of overall health of photosynthetic organisms including Symbiodiniaceae (Xiao *et al.*, 2022), did not provide a complete understanding of the overall photophysiological stress response in *B. minutum* strains used in this study. *Breviolum minutum* strains with two distinct ITS2 profiles (SCF-127 versus A2-6, A3-S12) showed different trajectories at all temperatures except for 40 °C where the data converged (Fig. 3B–D). A2-6 and A3-S12 had similar trajectories at all temperatures (Fig. 3B–D). The non-photochemical parameters, Y(NPQ) and Y(NO), also showed contrasting trends for SCF-127 versus A2-6 and A3-S12, whereas A2-6 and A3-S12 (same ITS2 profile) were similar to each other (Fig. 3D, E). Y(NPQ) and Y(NO) data were significantly ($P\leq0.0001$ for both parameters) different in SCF-127 compared with A2-6 and A3-S12 across the temperature range 26, 28, 30, 32, 33 and 34 °C (Fig. 3D, E). The distinct photophysiological behaviour of SCF-127 was also reflected in an ~1.4-fold ($P<0.0001$) higher E_k value compared with A2-6 and A3-S12 (Supplementary Table S2). The differences in the photophysiological behaviour between SCF-127 (35.37 °C), and A2-6 (33.99 °C), A3-S12 (34.02 °C) nearing their thylakoid melting temperatures (34 and 35 °C) mainly arose from variations in coefficients of non-photochemical components such as Y(NO), Y(NPQ) (Fig. 3A, D, E), qN (Supplementary Fig. S5C), and NPQ_{SV} (Fig. 4, Supplementary Table S3). Overall, a significant interaction effect between short-term temperature exposure and *B. minutum* strains across all photosynthetic parameters except F_m was observed (Supplementary Table S1). Significant differences in photosynthetic behaviour of *B. minutum* strains with distinct ITS2 profiles (SCF-127 versus A2-6, A3-S12) were observed

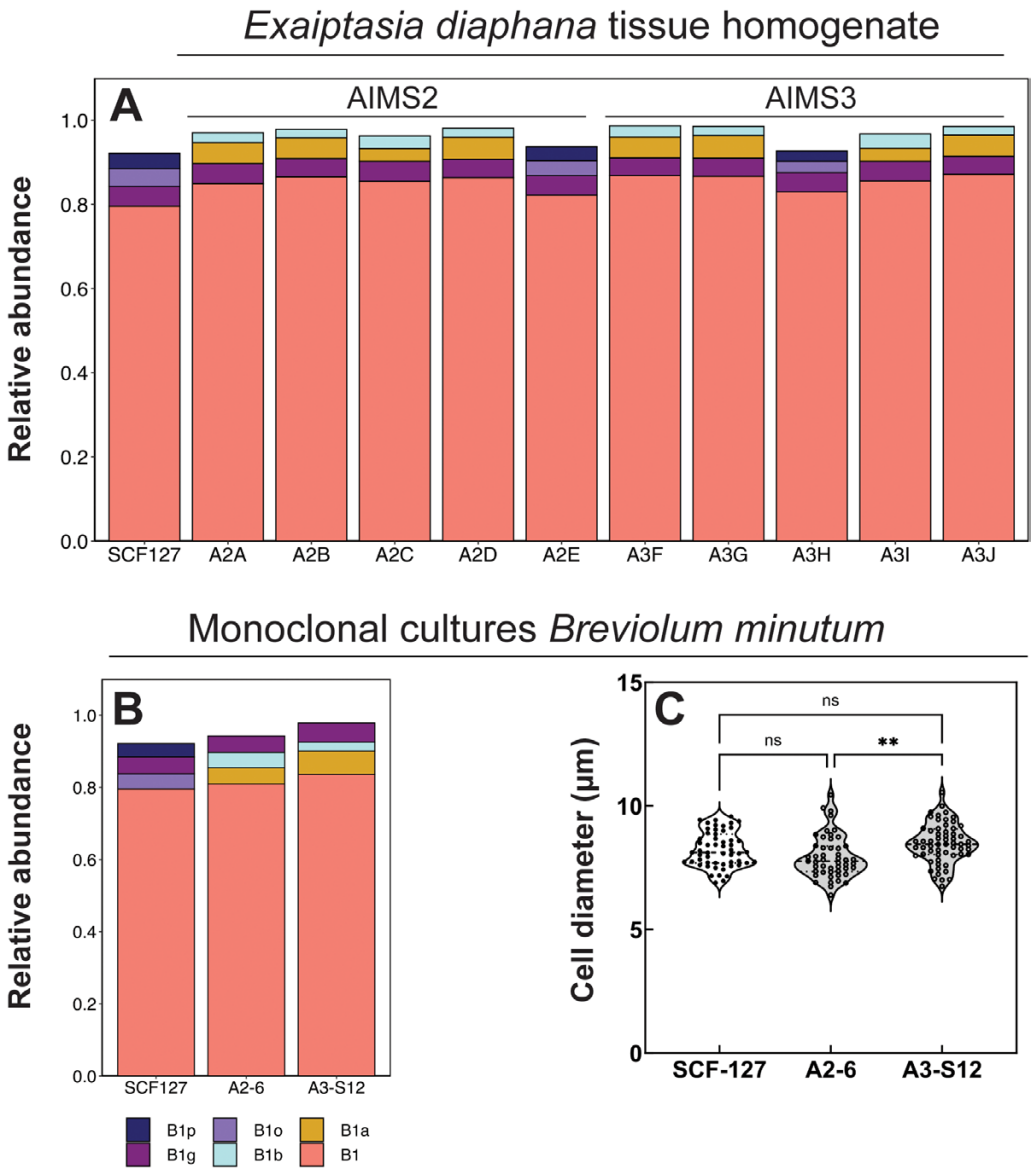

Fig. 1. Characterization of *Breviolum minutum* strains. (A) ITS2 profiles of endosymbiont communities of *Exaiptasia diaphana* (genotypes AIMS2 and AIMS3, abbreviated as A2 and A3; letters A–I indicate different clones). (B) Cultured monoclonal isolates: SCF-127, ITS2 profile: B1–B1o–B1g–B1p; and A2-6, A3-S12, ITS2 profile: B1–B1a–B1b–B1g. (C) Mean cell diameter (µm) of monoclonal isolates. Cell numbers (*n*) for cell diameter estimations were 55, 49, and 66 for SCF-127, A2-6, and A3-S12, respectively. Coloured squares represent different ITS2 profiles and bars in (A, B) and are arranged based on relative abundance. ***P*=0.0011, where level of significance is 0.05.

as temperature approached the thylakoid membrane thermal melting point for the latter two strains (33.99 °C and 34.02 °C, respectively; Supplementary Table S3).

Photoprotective mechanisms—Stern–Volmer non-photochemical quenching, de-epoxidation state, and reactive oxygen species

The levels of NPQ_{SV} at ambient temperature (26 °C) and its trends with increasing temperature were starkly different in *B. minutum* strains represented by the two distinct ITS2 profiles (Fig. 4). At ambient temperature (26 °C), SCF-127 showed ~80% lower levels of NPQ_{SV} compared with A2-6 (P=0.0006) and A3-S12 (P=0.0005) (Supplementary Table S4), which is consistent with the observed levels of Y(NPQ) (Fig. 3) and qN (Supplementary Fig. S5C). The levels of NPQ_{SV} (Fig. 4A) and qN (Supplementary Fig. S5C) dropped at 28 °C and 30 °C and steadily increased as temperature rose in SCF-127 cultures. Conversely, in A2-6 and A3-S12 these parameters showed declining trends until the thylakoid membrane thermal melting point (~34 °C) and increased thereafter (Fig. 4B, C). Significant differences were observed between *B. minutum* strains across

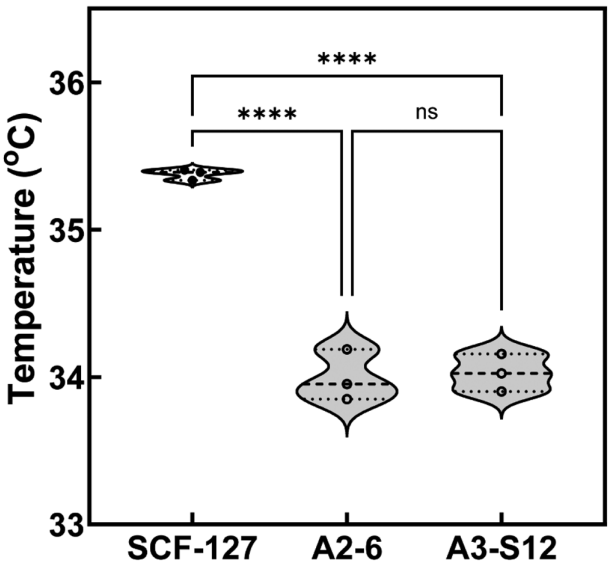

Fig. 2. The thermal melting point of thylakoid membrane in three *B. minutum* strains. SCF-127 has the ITS2 profile B1–B1o–B1g–B1p, and A2-6 and A3-S12 are B1–B1a–B1b–B1g. Data points indicate estimated melting temperatures of thylakoid membranes based on Weibull's equation using maximum photosynthetic yield of photosystem II (F_v/F_m) under rapid short-term cumulative temperature stress. ****P<0.0001 where the level of significance was 0.05 (n=3 per strain).

all parameters associated with activation of photoprotective mechanisms under increasing rapid short-term cumulative heat stress (Supplementary Table S4).

Pigment accumulation

The DES is governed by the accumulation of two pigments (ratio of Dtx to Ddx) and facilitates NPQ formation (Roháček *et al.*, 2014), maintains integrity of the thylakoid membrane (Bojko *et al.*, 2019), and is hypothesized to play a role in ROS scavenging (Lepetit *et al.*, 2010). A strong positive linear correlation was observed between NPQ_{SV} and DES (R^2=0.802, Supplementary Fig. S6) with increasing temperature exposure only in SCF-127 cultures (Fig. 4A). In A2-6 and A3-S12, the DES was several-fold lower across all temperatures compared with SCF-127 (Fig. 4B, C). However, this was not correlated with NPQ_{SV} levels (Supplementary Fig. S6). At 40 °C, the DES was significantly elevated in all three strains (SCF-127: 32.2 ± 4%, P<0.0001; A2-6: 33.4 ± 10%, P=0.0003; and A3-S12: 52.3 ± 5%, P<0.0001; Dunnett's multiple comparison test) compared with 26 °C (Fig. 4).

Formation of reactive oxygen species

At all temperature exposures, SCF-127 and A3-S12 (Fig. 4A, C) consistently accumulated more ROS compared with A2-6. (Fig. 4B). Although a strong interaction effect was found between temperature and *B. minutum* strains for formation of ROS (P<0.0001, F(14,42)=9.201) (Supplementary Table S5), no clear trend in ROS levels was observed with increasing temperature exposure across all three strains (Fig. 4; Supplementary Table S5).

Resolution of components of non-photochemical quenching (relaxation) under heat stress

The differences between the strains from two *B. minutum* ITS2 profiles were reflected in the trend of activation of dynamic components of NPQ (Fig. 5; Supplementary Table S6). At ambient temperature (26 °C), SCF-127 showed lower levels of energy-dependent quenching (fast relaxing qE type; Fig. 5A) and light harvesting complex II (LHCII) attached to PSII (state transition qT_1 type; Fig. 5C) and higher levels of LHCII reorganization around PSI (state transition qT_2 type NPQ, Fig. 5D) compared with A2-6 and A3-S12. At 40 °C, all three strains showed elevated qE type NPQ values. The value was most elevated relative to 26 °C in SCF-127 (by 98.3 ± 0.02%, P<0.0001; Dunnett's multiple comparison test) (Fig. 5A), but only marginally elevated in A2-6 and A3-S12 (by 11 ± 0.02%, P=0.0008, and 1.75 ± 0.008%, respectively, Dunnett's multiple comparison test). In A2-6 and A3-S12, the qE component was deactivated with increasing temperature up to 34 °C (Fig. 5A). Trends in the activation of the qI type NPQ (energy quenching due to photoinhibition) were similar in all cultures up to 32 °C, when SCF-127 showed a significantly increased activation compared with A2-6 and A3-S12 (Fig. 5B; Supplementary Table S6).

The components associated with the state transition of LHCII from PSII to PSI are qT_1 and qT_2 type NPQ, respectively, and they are observed under dark relaxing recovery conditions following induction under actinic illumination. The trend in activation of these components was different in SCF-127 compared with A2-6 and A3-S12 (Fig. 5C, D). The levels of qT_1 remained significantly lower in SCF-127 up to 32 °C compared with the other strains (F(14,42)=20.41, P<0.0001; Fig. 5A) and increased by ~50–60% as temperature approached the thylakoid membrane thermal melting point (35.37 °C) for this strain (Fig. 5C). Conversely, qT_2 levels in A2-6 and A3-S12 were consistently lower compared with SCF-127 across all temperatures (F(14,42)=94.83, P=0.0001; Fig. 5D). A2-6 and A3-S12 also showed a sustained increase in activation of the qT_2 component as the temperature approached the thylakoid membrane thermal melting point (~34 °C) for these strains (Fig. 5D). Overall, SCF-127 showed a high and sustained photoprotective response that was distinct from that of A2-6 and A3-S12 cultures (Supplementary Fig. S5; Supplementary Table S6). The latter two cultures showed full relaxation of NPQ_{SV} under dark conditions except at ambient (26 °C) and elevated temperatures (40 °C) (Supplementary Fig. S5). Overall, qE type NPQ relaxation was mostly operational in A2-6 and A3-S12 whereas qT_2 type NPQ relaxation was dominant in SCF-127 (Fig. 5A, D). A strong interaction

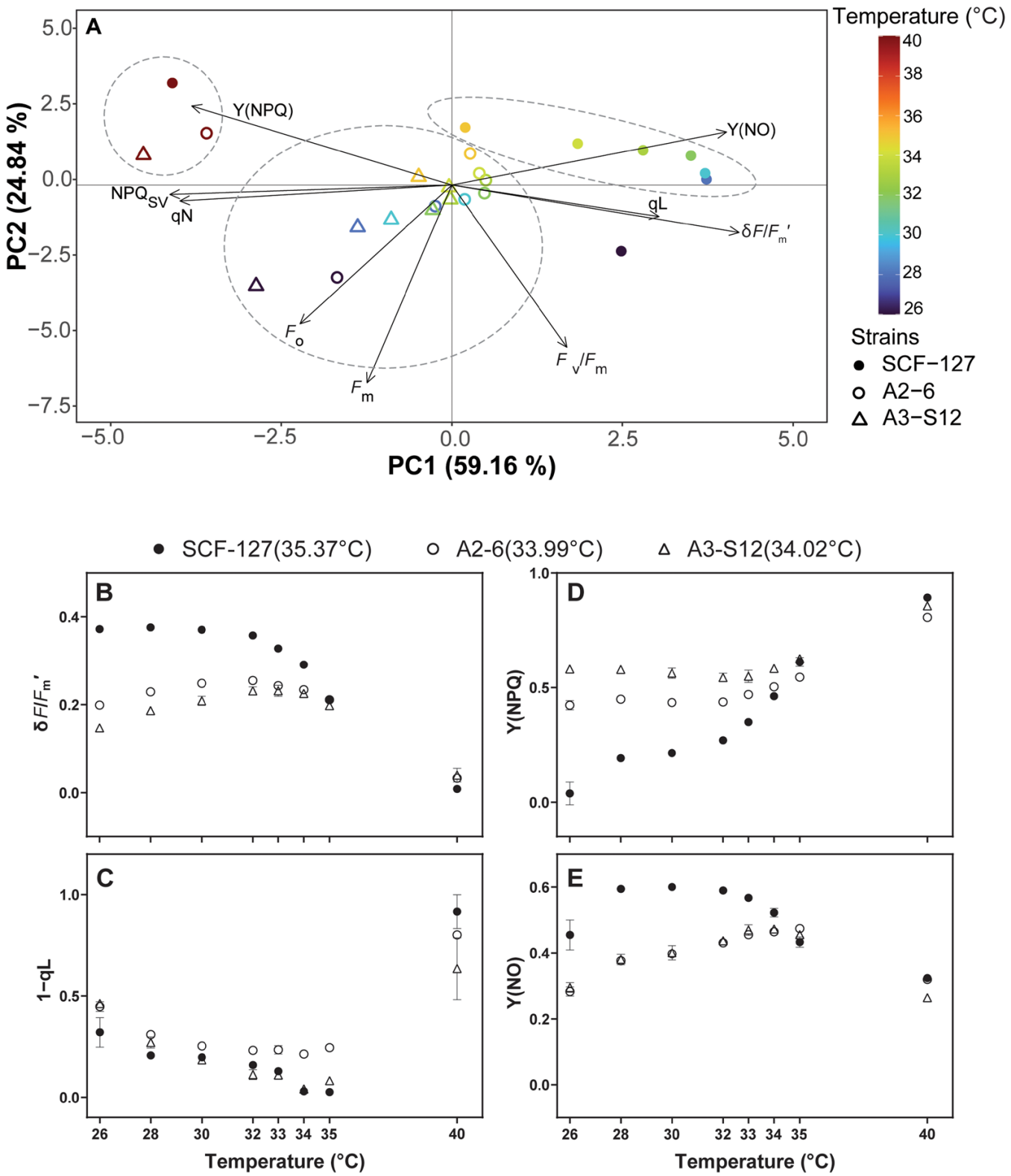

Fig. 3. Changes in photosynthetic parameters of photosystem II in the three *B. minutum* strains as a function of rapid short-term cumulative temperature stress (26–40 °C). (A) Principal component analysis (bi-plot) of various photosynthetic parameters associated with *B. minutum* strains exposed to increasing temperatures (coloured scale). Dashed ellipses and circle indicate grouping of strains and extreme temperature (40 °C) along PC1. (B–E) Differences in photochemical $\delta F/F_m'$ (B) and 1−qL (C) and non-photochemical Y(NPQ) (D) and Y(NO) (E) coefficients. Temperature values in (B–D) are the thylakoid membrane thermal melting points of the *B. minutum* strains. Data points are means ±SD, *n*=3 per strain.

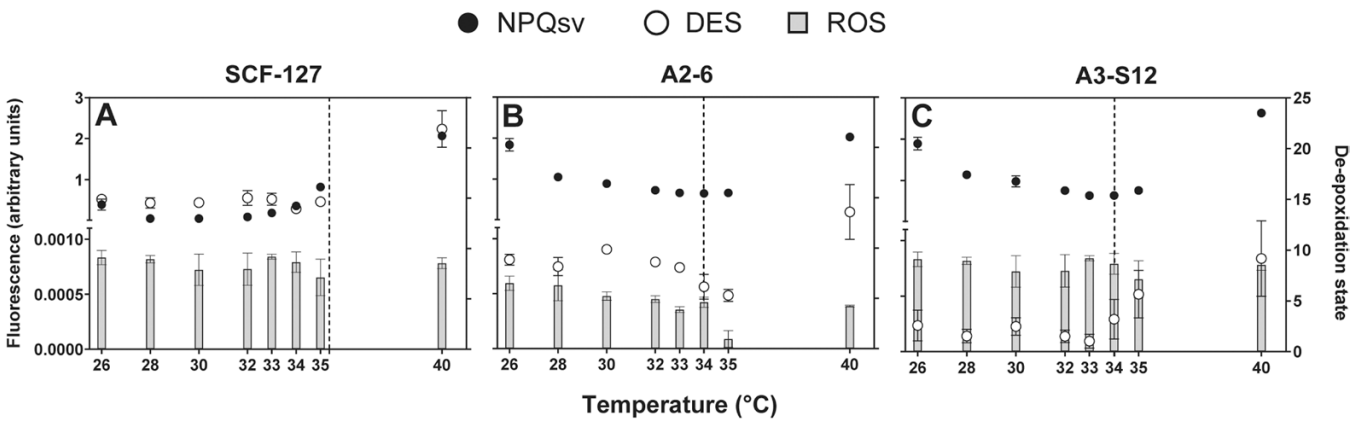

Fig. 4. Activation of photoprotection response in three strains of *B. minutum*. Photoprotective response comprised of Stern–Volmer non-photochemical quenching (NPQ_{SV}), reactive oxygen species (ROS, $cell^{-1}$) and de-epoxidation state (DES) in three *B. minutum* strains, SCF-127 (A), A2-6 (B), and A3-S12 (C), as a function of rapid short-term cumulative heat stress (26–40 °C). Vertical dashed lines are the thermal melting point of the thylakoid membranes for each *B. minutum* strain. The bottom and top halves of the *y*-axis show ROS and NPQ_{SV} datasets. The right *y*-axis shows DES, which is a ratio of diatoxanthin to diadinoxanthin pigments. Values on both *y*-axes are arbitrary units. Data points are means ±SD, *n*=3 per strain.

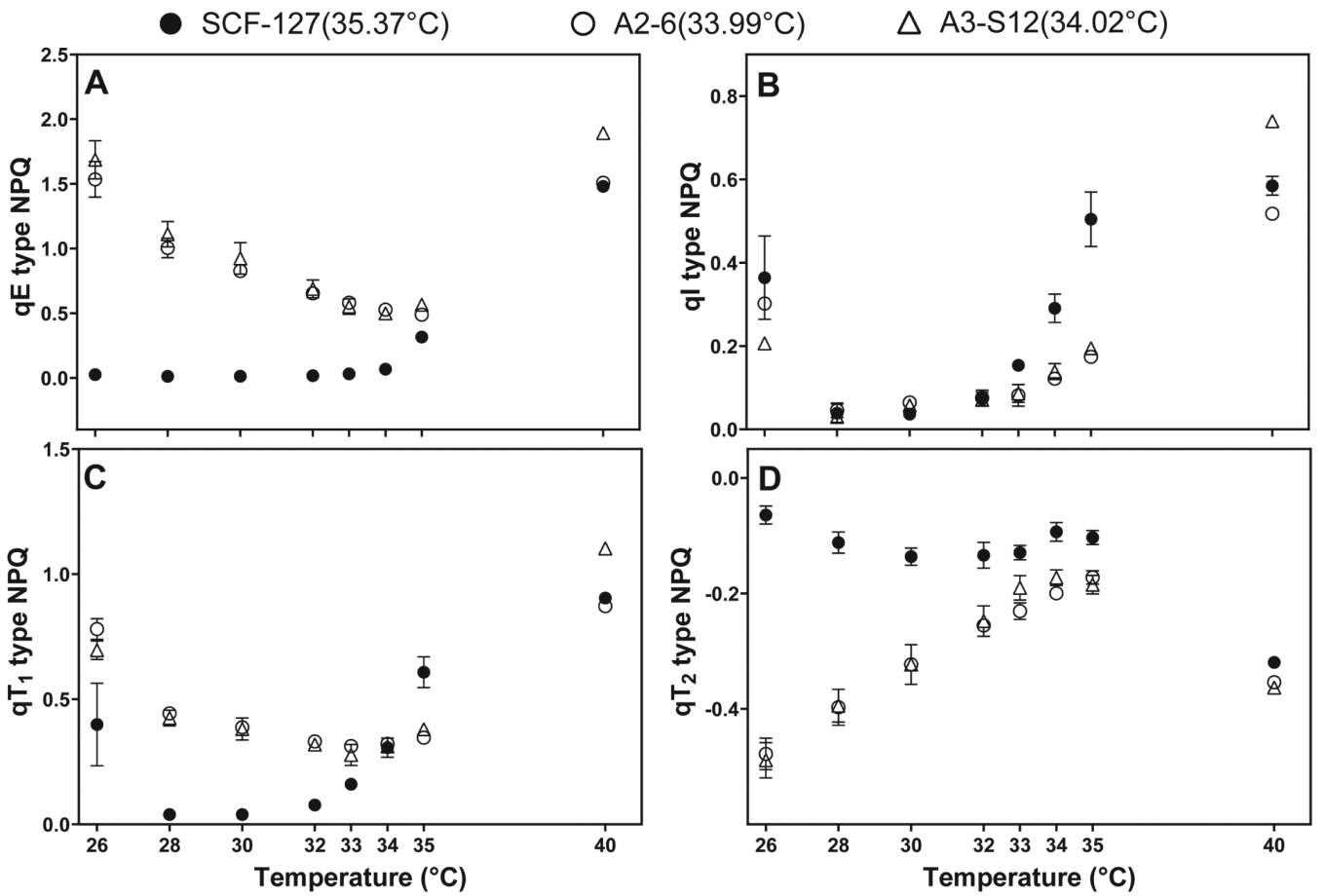

Fig. 5. Dynamic resolution of components of NPQ in three *B. minutum* strains. (A) qE type or fast relaxing; (B) qI or slow relaxing; (C) qT_1; and (D) qT_2 type. Temperature values in the legend above graphs are the thermal melting points of thylakoid membranes for each *B. minutum* strain. Data points are means ±SD, *n*=3 per strain.

effect was observed between strains of *B. minutum* belonging to distinct ITS2 profiles and temperature for all resolved components of NPQ relaxation (qE, qI, qT_1, and qT_2 type) (Supplementary Table S6).

Components of non-photochemical quenching (relaxation) in presence of metabolic inhibitors

There was a difference in the levels of inhibition of the qE component of NPQ between the *B. minutum* strains characterized by the two ITS2 profiles ($F(6,18)=28.11$, $P<0.0001$; Fig. 6A; Supplementary Table S7) when exposed to chemical inhibitors such as ammonium chloride (NH_4Cl; disrupts the pH gradient across the thylakoid membrane), dithiothreitol (DTT; inhibitor of de-epoxidation reaction) and diphenyleneiodonium chloride (DPI; inhibitor of epoxidation reaction). NH_4Cl- and DTT-treated cultures showed large reductions in qE levels in all three strains compared with the control (no chemical exposure) and the DPI-treated group (Fig. 6A; Supplementary Table S8). In the DTT-treated group the levels of qE inhibition were statistically different only between SCF-127 and A3-S12 ($P=0.0046$; Supplementary Table S7). The qI component of NPQ was significantly inhibited in SCF-127 ($P=0.0043$) and A2-6 ($P=0.0102$) treated with DTT compared with the control (Supplementary Table S8); however, no significant differences were observed between *B. minutum* strains (Supplementary Table S7). In DPI-treated cultures, the qI type NPQ component was reduced in SCF-127 (by $22.46 \pm 4.7\%$, $P=0.0452$) compared with A3-S12; however, its level was not significantly different from the control (Fig. 6B; Supplementary Tables S7, S8).

The levels of qT_1 and qT_2 were significantly ($P<0.0001$) inhibited in the DTT-treated cultures compared with the controls (Fig. 6C, D). The levels of qT_2 were also impacted in SCF-127 ($P=0.0119$) and A2-6 ($P=0.0847$) in the presence of NH_4Cl compared with the control (Fig. 6D; Table Supplementary S8). Inter-strain differences were observed for the levels of qT_1 and qT_2 type NPQ inhibition in NH_4Cl and DPI treatments but not in DTT-treated groups (Fig. 6C, D). The values for qE and qI components of NPQ (at 26 °C in Fig. 5A, B and for control Fig. 6A, B) are different, although they follow a similar trend. Specifically, qE levels are lowest in SCF-127 whereas qI levels are similar for SCF-127 and A2-6. The trend of qT_1 and qT_2 components (at 26 °C in Fig. 5C, D and for control Fig. 6C, D) were different.

Discussion

Thermal stress responses of the three *B. minutum* cultures representing two distinct ITS2 profiles

We used a rapid short-term cumulative temperature exposure (26–40 °C) to evaluate differences in the upper thermal tolerance limits in three strains of *B. minutum*, which represent two ITS2 profiles. Thus, this experiment is unlike commonly used long-term elevated temperature studies in which ambient and elevated treatments are run separately for the same duration (Dungan *et al.*, 2020, 2022), often with acclimation at a specific temperature prior to elevating the temperature. Rapid short-term cumulative stress experiments, similar to this study, are often used for screening basal thermal tolerance levels in genetic variants of Symbiodiniaceae (Díaz-Almeyda *et al.*, 2011, 2017; Mansour *et al.*, 2018; Russnak *et al.*, 2021). Such rapid and reproducible experiments provide a reliable and high throughput method for understanding the photobiological potential and basal thermal tolerance (Ilík *et al.*, 2018) levels of strains. However, rapid short-term cumulative experiments do not provide insight into the adaptive potential of strains (Ilík *et al.*, 2018), or possible growth-related trade-offs (Scharfenstein *et al.*, 2023). The photobiological behaviour of an organism is dependent on previous light exposure conditions (Serôdio *et al.*, 2013) (hysteresis), the effect of which remains unresolved in rapid short-term cumulative temperature experiments.

This study employed a widely used molecular marker, ITS2, to delineate *B. minutum* strains. Despite its common use, it is challenging to distinguish between sequences that reflect intragenomic versus intergenomic variation within the ribosomal cistron of Symbiodiniaceae, unless accompanied by other chloroplast and mitochondrial marker assays, e.g. chloroplast large-subunit (cp23), *psbA* gene on plastid minicircle non-coding region ($psbA^{ncr}$) for D1 protein of PSII and mitochondrial cytochrome *b* (*cob*) (Davies *et al.*, 2023). The three monoclonal cultures (SCF-127, A2-6, and A3-S12) used in this study were determined to be strains of *B. minutum* having two distinct ITS2 profiles (SCF-127, B1–B1o–B1g–B2p; and A2-6 and A3-S12, B1–B1a–B1b–B1g). Dungan *et al.* (2020, 2022) reported that the *E. diaphana* genotype AIMS2 exclusively harboured B1–B1o–B1p profile *B. minutum* (different from the ITS2 profiles of the cultures used here) whereas AIMS3 was predominantly colonized by B1–B1a–B1b (as for A2-6 and A3-S12) and some clones of AIMS3 also contained low levels of ITS2 profile B1–B1o–B1p (different from the ITS2 profiles of the cultures used here). Such different ITS2 profiles could arise due to complete and/or incomplete concerted evolution (Figueroa *et al.*, 2021; Wang *et al.*, 2023) or possible symbiont shuffling (Baker, 2003) of *B. minutum* strains over time in *E. diaphana*. We observed that *B. minutum* strains belonging to two different ITS2 profiles showed consistent differences in their photophysiological functional responses under increasing temperature. A2-6 and A3-S12 had similarities in the thermal melting point of their thylakoid membrane, photopigment accumulation, and various photophysiological parameters, which were distinct from functional responses of SCF-127.

The functional variability in plastid traits such as the thermal melting point of the thylakoid membranes (Díaz-Almeyda *et al.*, 2011; Mansour *et al.*, 2018) in *B. minutum* strains (Russnak *et al.*, 2021) has previously been reported. Our results corroborate

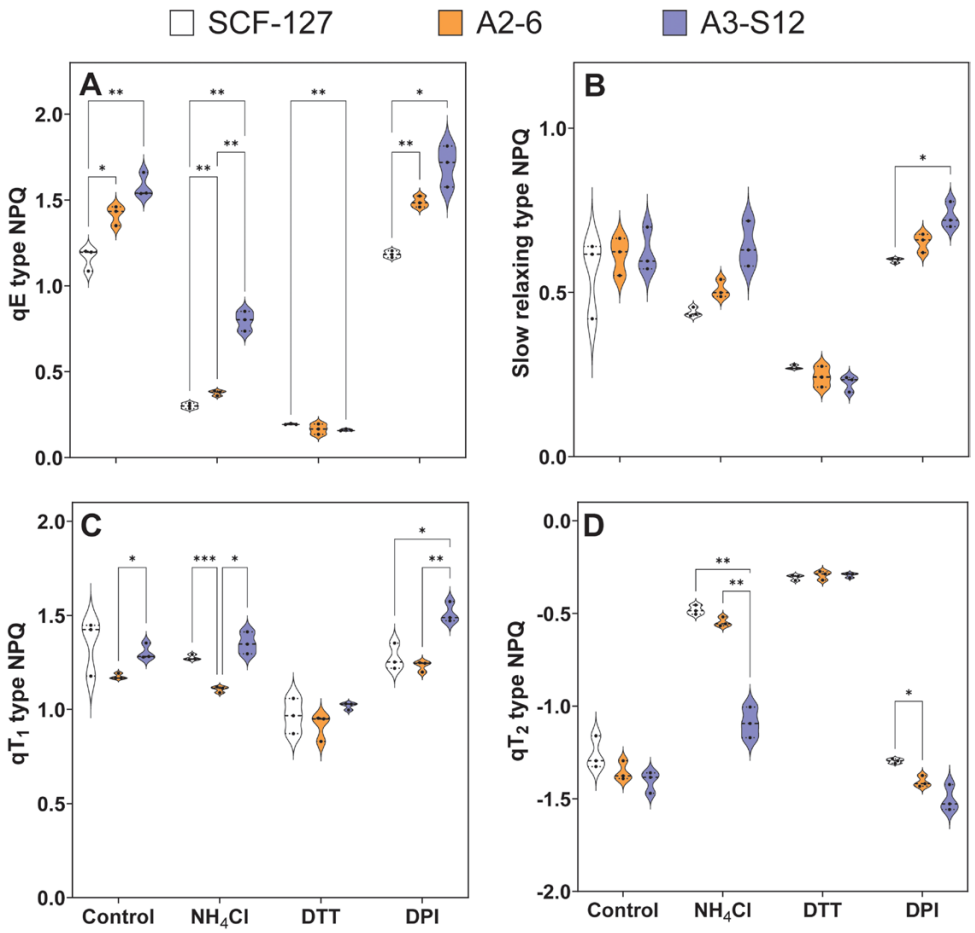

Fig. 6. Dynamic resolution of components of NPQ in presence of metabolic inhibitors in three *B. minutum* strains. qE type or fast resolving (A), qI or slow relaxing (B), qT_1 type (C) and qT_2 type (D) components of NPQ in the presence of inhibitors ammonium chloride (NH_4Cl, 5 mM), dithiothreitol (DTT, 1 µM) and diphenyleneiodonium chloride (DPI, 1 µM). Control indicates untreated cultures and data points inside violin shaped features are values for each replicate; thick dashed line is median and thin dashes are minimum and maximum; n=3 per strain. Asterisks *, **, and *** indicate P value<0.0032, 0.0021, and 0.0002, respectively.

the earlier findings that the differences in functional responses under thermal stress are strongly linked to genetic relatedness among *B. minutum* strains. We found *B. minutum* SCF-127 is of a similar ITS2 profile to that previously reported in *E. diaphana* genotype AIMS2 (Dungan *et al.*, 2020, 2022), where its presence in the anemone host correlated with higher host bleaching tolerance when it was subjected to elevated temperature (Dungan *et al.*, 2022) and light (Dungan *et al.*, 2020). We found higher thermal tolerance *in vitro* in SCF-127 when compared with strains A2-6 and A3-S12. This suggests that the higher thylakoid membrane melting point of SCF-127, an indicator of thylakoid membrane fluidity, might better preserve the function of the membrane-embedded photosynthetic apparatus (Díaz-Almeyda *et al.*, 2011).

At ambient temperature (26 °C), the higher E_k, an indicator of minimum saturation irradiance, in SCF-127 suggest its high photoacclimation potential (active photochemistry) over a wide range of high light intensities (Ralph and Gademann, 2005). This finding is in agreement with previous research (Dungan *et al.*, 2020) wherein the clones of *E. diaphana* (AIMS2) harbouring *B. minutum* with a similar ITS2 profile to SCF-127 showed rapid recovery upon exposure to increased light intensities, whereas clones harbouring different *B. minutum* strains did not. The lower E_k in A2-6 and A3-S12 suggests that components of NPQ largely dominated the energy quenching and are likely to be a preferred photoprotection strategy in these strains. This corroborates the higher levels of overall NPQ_{SV} observed even at ambient temperature (26 °C) in A2-6 and A3-S12. The thylakoid membrane thermal melting point is species- and strain-specific and was previously reported to be in the range 36.5–42 °C for *B. minutum* (Díaz-Almeyda *et al.*, 2011; Mansour *et al.*, 2018), which is higher than we observed for the Great Barrier Reef strains (33.99, 34.02, and 35.37 °C).

Stress photophysiology of *B. minutum* strains (SCF-127 versus A2-6 and A3-S12)

An energetic coupling between photosynthesis and respiration strongly regulated by temperature has been reported in

species of *Symbiodinium*, *Durusdinium*, and *Effrenium*; however, this was not the basis of long-term adaptive heat stress responses (Pierangelini *et al.*, 2020). In our study, we found that short-term elevation in temperature instead leads to differential activation of a range of photoprotective mechanisms, collectively referred to as NPQ, which is made up of qE and the state transition qT_1 and qT_2 (Herdean *et al.*, 2023). It also caused the closure of photosynthetic reaction centres (1−qL) and de-epoxidation of Ddx to Dtx. Importantly, the trends and absolute levels of these features are contrasting in our two ITS2 profile *B. minutum* strains, which indicates the possibility of a different operational energy balancing mechanism in them.

Quenching of fluorescence under heat stress

The increase in levels of F_o (Supplementary Fig. S5A) in A2-6 and A3-S12 compared with SCF-127, especially at the beginning of the temperature ramping when chlorophyll *a* concentrations in the strains were similar, is likely associated with reduced efficiency of electron transport across PSII (Maxwell and Johnson, 2000). This is also reflected in the overall reduced maximum relative electron transport rate values in A2-6 and A3-S12 compared with SCF-127 (Table Supplementary S2). The decline in F_v/F_m values (which are also dependent on F_o levels) as well as $\delta F/F_m'$ (an indicator of photosynthetic yield of PSII in the light) (Klughammer and Schreiber, 2008; Schreiber and Klughammer, 2008) with increasing temperature (26–40 °C) in the two ITS2 profile *B. minutum* strains is either due to the damage to PSII reaction centres (Schreiber, 2004), the D1 protein, or the closure of PSII reaction centres (1−qL) (Murchie and Lawson, 2013). The latter is unlikely to have played a role, because the 1−qL parameter, which is an indicator of the fraction of closed reaction centres (Oxborough and Baker, 1997; Kramer *et al.*, 2004), remained low and increased only after the temperature exceeded the thermal melting point of thylakoid membrane for each ITS2 profile (Fig. 3C). Although the levels of F_o did not significantly decline in SCF-127, its slight decline (but non-significant change) in A2-6 and A3-S12 over increasing temperatures indicates changes in plastoquinone pool and a possibility of chlororespiration (Chemeris *et al.*, 2004). The declining trend in F_m levels is linked to activation of different components of NPQ (qE and the state transition, qT_1 and qT_2) participating in the photoprotective response (Allorent *et al.*, 2013; Roháček *et al.*, 2014; Herdean *et al.*, 2023). Therefore, the elevation of qE (fast relaxing component of NPQ) in A2-6 and A3-S12, and Y(NO) (unregulated heat loss) in SCF-127 is the probable cause for the reduction in F_m levels.

Differences in photoprotective mechanisms

Pigment-independent activation of NPQ in A2-6 and A3-S12

Activation of the qE component is widely reported to be driven by acidification of the thylakoid lumen (Müller *et al.*, 2001), which leads to protonation of the proteins PsbS (Wilk *et al.*, 2013; Ros, 2020) and diadinoxanthine de-epoxidase (Venn *et al.*, 2006); the latter converts Ddx to Dtx and the former is a membrane protein that in combination with Dtx forms a quenching complex that suggests assistance in the dissipation of extra energy as heat (NPQ) (Lepetit *et al.*, 2010). Our study validated the possible abolishment of NPQ using metabolic inhibitors: NH_4Cl, which eliminates the pH gradient across the thylakoid membrane, and DTT and DPI, which inhibit de-epoxidation (Ddx to Dtx conversion in light) and epoxidation (reversal of Dtx to Ddx in dark), respectively (Roháček *et al.*, 2014). The DPI treatment showed no significant difference in components of NPQ compared with control (except for the qT_2 parameter in A3-S12). This suggests that the re-conversion of Dtx to Ddx is mediated by a different kind of enzyme or does not occur in *B. minutum*. The differences in values of qT_1 and qT_2 components (at 26 °C in Fig. 5C, D and for control in Fig. 6C, D) likely arose from differences in the metabolic state of the cultures (Rochaix, 2014) as the data presented in Figs 5, 6 were collected from separate experiments (batch cultures).

In *B. minutum*, Dtx (de-epoxidated from Ddx under high light) is reported to accumulate in the thylakoid membranes and in the LHC of PSI (Kato *et al.*, 2020). The reduced levels of Dtx in A2-6 and A3-S12 likely resulted from inhibition of the de-epoxidase reaction. Significant levels of inhibition of the de-epoxidation reaction in the presence of its metabolic inhibitor, DTT (Müller *et al.*, 2001), was observed for the qE component of NPQ in A3-S12 (P=0.0046) but not in SCF-127 (Supplementary Table S7). This observation is in line with our expectations because of the dependency of the qE component on the quenching complex containing Dtx (Lepetit *et al.*, 2010). Reduction in Dtx (using an inhibitor) in the diatom *Phaeodactylum tricornutum* was reported to negatively influence activation of NPQ (Roháček *et al.*, 2014). However, contrary to our expectations, the overall levels of NPQ_{SV} were not linearly correlated with the DES (ratio of Dtx to Ddx) in A2-6 and A3-S12 (Supplementary Fig. S6), although the qE type component was most dominant (Fig. 5A). This hints at the presence of an alternative, pigment-independent mechanism for qE type NPQ activation. A similar strategy for qE activation in the absence of de-epoxidized pigments was observed in *npq1* mutants of the algae *Chlamydomonas reinhardtii* (Bonente *et al.*, 2011), *Tetracystis aeria*, and *Pedinomonas minor* (Quaas *et al.*, 2015), and in some members of the *Bryopsidales* (Christa *et al.*, 2017). It has been hypothesized that pigment-independent activation of qE is due to the presence of a different enzyme similar to de-epoxidase (Christa *et al.*, 2017). The reduction in qE and qT_2 levels (dependent on the Dtx pool) compared with controls in the presence of metabolic inhibition with DTT suggests that Ddx de-epoxidase is present in all three *B. minutum* strains. This highlights the possibility that a Dtx-independent quencher site, similar to LhcSR3 in *C. reinhardtii* (Bonente *et al.*, 2011), is present in A2-6 and A3-S12. We suggest a complete characterization of photopigments and

proteins in all strains of *B. minutum* is essential for the validation of potential sites of energy quenching.

Pigment-dependent activation of NPQ in SCF-127

In SCF-127, the positive correlation between NPQ_{SV} and the DES (Supplementary Fig. S6) suggests a pigment-dependent qE type component is likely to be operational; however, its levels were minimal compared with A2-6 and A3-S12. Similar observations were outlined by Lepetit *et al.* (2010) demonstrating high light induced accumulation of Dtx in the diatom *P. Tricornutum*, with no observable levels of qE type NPQ. This suggests that the accumulated Dtx likely has an additional physiological role, especially under increasing temperature stress that is otherwise known to activate a qE-mediated photoprotective responses in many other algal species (Goss and Lepetit, 2015). Dtx is present in the lipid shield (composed of monogalactosyldiacylglycerol, which is also part of thylakoid membrane) around the LHC in diatoms (Lepetit *et al.*, 2010) and PSI–LHC supercomplex in *B. minutum* (Kato *et al.*, 2020). Incorporation of Dtx in thylakoid membranes is implicated in short- and long-term membrane rigidification under elevated temperatures in *P. Tricornutum* (Bojko *et al.*, 2019), which indirectly prevents ROS leakage (Kihara *et al.*, 2014), lipid peroxidation and is hypothesized to act as an antioxidant (Lepetit *et al.*, 2010). Rodrigues *et al.* (2023) reports improved thermal tolerance in isoprene producing cyanobacteria and hypothesized that higher levels of xanthophyll pigments (equivalent to Dtx and Ddx in this article) improved thylakoid membrane fluidity. An increased amount of photoprotective pigments in the thermally tolerant strain (SCF-127) is in agreement with our observation. Consistently higher ROS accumulation in SCF-127 and its marginal fluctuations in A2-6 and A3-S12 (Fig. 4) under increasing temperature (30, 32, 33, 34, 35, and 40 °C) strongly suggests that the Dtx pool is essential for enhanced membrane rigidification, especially in SCF-127. This is corroborated by the higher thylakoid membrane melting point in SCF-127 (Fig. 2) indicating preservation of membrane integrity (rigidification) at temperatures 1.38 °C and 1.35 °C above those of A2-6 and A3-S12. Further, the increasing levels of qE type around the thylakoid membrane thermal melting point of SCF-127 (35.37 °C) indicate possible re-allocation of Dtx for efficient energy quenching under extreme temperature conditions.

Balancing of excess excitation energy as a part of the photoprotective strategy

The components of the qT type of NPQ are linked to state transitions that involve a reversible redistribution of LHCII from PSII (qT_1) to PSI (qT_2), essentially reducing the antenna size of the former to balance the excitation energy and minimize the photodamage (Allorent *et al.*, 2013). Attachment of LHCII to PSI, also known as 'super-quenching' (Slavov *et al.*, 2016), leads to the onset of cyclic electron flow, which is a well-known strategy employed by cultured Symbiodiniaceae cells of several genera under heat stress (Aihara *et al.*, 2016) and *B. minutum* in periods of high light exposure (Kato *et al.*, 2020). Low levels of qT_1 in SCF-127 (Fig. 5C) during the initial rise in temperature along with higher qT_2 (Fig. 5D) suggests active dissociation of LHCII (possibly containing Dtx) from PSII and attachment to PSI. This super-quenching redirects excitation energy from PSII to PSI (spill-over), which is hypothesized to indirectly participate in photoprotection (Kato *et al.*, 2020). High light stress conditions are reported to cause dissociation of LHCs in *Symbiodinium* spp. but not in *Breviolum* spp. under light stress (Reynolds *et al.*, 2008). Our observation on state transitions (qT_1 and qT_2) suggest that LHCII reorganization occurs in strains of *B. minutum* (especially in SCF-127) under elevated temperature conditions. Higher levels of state transitions and E_k in SCF-127 (Supplementary Table S2) hint at the possibility of high light tolerance in this strain. Exposure to elevated temperature and high light can synergistically impact Symbiodiniaceae *in hospite* (Coles and Jokiel, 1978; Sinutok *et al.*, 2022; Travesso *et al.*, 2023) and *ex hospite* (Díaz-Almeyda *et al.*, 2017). Therefore, the cumulative impact of these stress conditions on the photophysiology of Symbiodiniaceae needs to be investigated, especially for heat-tolerant strains (Buerger *et al.*, 2020). The possibility of formation of a super-quenching PSI site in SCF-127 is highly likely, and is often reported to be linked to elevated levels of non-regulated heat-dissipation Y(NO) (Kramer *et al.*, 2004) and PSII inactivity (Kato *et al.*, 2003). Our study corroborates this for Y(NO) as SCF-127 showed high Y(NO) levels.

Our data suggest that Dtx serves a dual photoprotective role in SCF-127, firstly by maintaining the integrity of the thylakoid membrane as an early response to heat, and subsequently, under extreme temperatures, the Dtx pool is incorporated in the quenching complex formation thereby allowing safe dissipation of excess energy (qE type NPQ). SCF-127 also employs cyclic electron flow around PSI in initial periods of heat stress to minimize photodamage (Dang *et al.*, 2019). The dynamic modulation of these features is a unique characteristic of the photoprotective mechanism employed by SCF-127 that underpins its higher thermotolerance compared with A2-6 and A3-S12. The lower levels of Dtx and thylakoid membrane melting point in A2-6 and A3-S12 underline that these strains have poor membrane rigidification and that the Dtx pool is solely allocated for activation of qE type NPQ. Inter-specific (Hill *et al.*, 2012) but not intra-specific variation (Aihara *et al.*, 2016) for activation of NPQ mechanisms driven by high light and temperature, respectively, has previously been reported. This study outlines detailed differences in photoprotective strategies under increasing temperature that were previously unknown in *B. minutum* strains with different ITS2 profiles (Fig. 7).

In conclusion, this study provides an in-depth understanding of the dynamic nature of different photoprotective components and their different activations among *B. minutum*

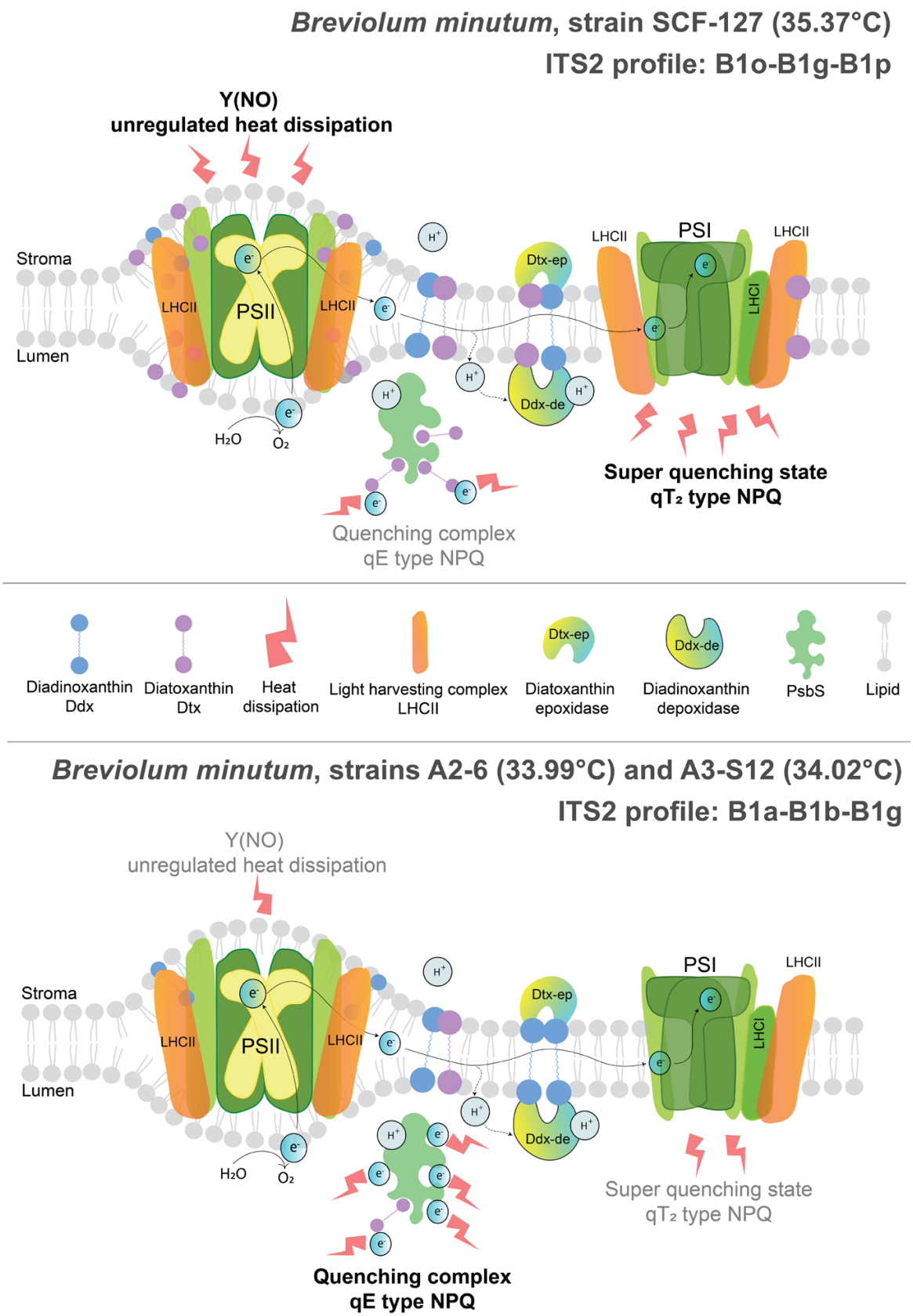

Fig. 7. Photoprotective mechanisms employed by the three closely related strains of *B. minutum*. SCF-127 (ITS2 profile B1–B1o–B1g–B1p, thylakoid melting point 35.37 °C) primarily dissipates energy through the super-quenching state (qT_2) and unregulated pathway Y(NO). SCF-127 also maintains a

higher level of membrane rigidity possibly by embedding more diatoxanthin (de-epoxidase from diadinoxanthin) into the thylakoid lipid bilayer. The other strains, A2-6 and A3-S12 (ITS2 profile B1–B1a–B1b–B1g, thylakoid melting points 33.99 and 34.02 °C, respectively), predominantly dissipate heat through the fast relaxing mechanism (qE) possibly mediated by a quenching complex that contains minimal levels of diatoxanthin. Differences in the number of heat dissipation (red), diadinoxanthin (blue dumbbell) and diatoxanthin (purple dumbbell) symbols indicate relative differences in the magnitude of photoprotective processes among *B. minutum* strains.

strains with distinct ITS2 profiles under rapid short-term cumulative heat stress (26–40 °C). Importantly, the different photoprotective mechanisms of SCF-127 versus A2-6 and A3-S12 are consistent with the previously observed thermal bleaching tolerance of their native host, *E. diaphana* (Dungan *et al.*, 2020, 2022). The commonly used indicators of heat tolerance, F_v/F_m, and antioxidant profiles provide a limited view of overall thermal robustness of Symbiodiniaceae. The heat-induced changes in the more thermally tolerant strain (SCF-127) compared with A2-6 and A3-S12 mainly included enhanced membrane rigidification along with an increased pool of Dtx pigments and a quick state transition of photosystems leading to a super-quenching state formation. A robust response to heat stress involves an intricate balance of mechanisms that process excitation energy without impacting the synthesis of essential metabolic products. We demonstrate that inter-strain variation in the upper thermal tolerance limits exists, with SCF-127 having a slightly higher thermal tolerance compared with A2-6 and A3-S12, but such differences are largely overlooked in the field.

Supplementary data

The following supplementary data are available at *JXB* online.

Fig. S1. Experimental design outlining rapid short-term cumulative heat stress.

Fig. S2. Optimization of determination of reactive oxygen species (ROS) levels using H_2DCFDA dye.

Fig. S3. A representative chromatogram of pigments extracted from *B.* minutum.

Fig. S4. Weibull's fitting for determination of thermal melting point thylakoid membranes in *B. minutum* strains.

Fig. S5. Change in photosynthetic parameters of PSII in *B. minutum* strains.

Fig. S6. Correlation between de-epoxidation state (DES) and non-photochemical quenching (NPQ_{SV}).

Table S1. Interaction effects between strains and exposure temperature (26–40 °C) for changes in photosynthetic parameters.

Table S2. Differences in rapid light curve fitting parameters [α, maximum relative electron transport rate ($rETR_{max}$) and E_k] compared between strains.

Table S3. Pairwise comparisons between the *B. minutum* strains for changes in all photosynthetic parameters nearing thylakoid melting temperatures, 34 °C and 35 °C.

Table S4. Pairwise comparisons between strains for changes in photoprotective parameters, NPQ_{SV}, de-epoxidation state (DES) and reactive oxygen species (ROS), under temperature stress (26–40 °C).

Table S5. Differences in ROS levels under elevated heat stress (28–40 °C) with respect to ambient temperature (26 °C).

Table S6. Pairwise comparisons between the strains for changes in NPQ components over rapid short-term cumulative heat stress (26–40 °C).

Table S7. Pairwise comparisons between the *B. minutum* strains for changes in NPQ components in presence of metabolic inhibitors.

Table S8. Comparison between control and inhibitor treatment groups for changes in components of NPQ.

Acknowledgements

Authors would like to acknowledge Dr Hugo Scharfenstein for help in modification of iPAM setup and Dr Ashley Dungan for scientific discussion related to ITS2 profiles of the strains.

Author contributions

PD, LLB, and MJHvO: conceptualization; PD: methodology; PD, MRN, and SJTMC: formal analysis and visualization; PD, MRN, and DR: investigation and data curation; MRN, DRB, EH LLB, and MJHvO: resources; PD, LLB, and MJHvO: funding acquisition; PD, MRN, and DR: writing—original draft; SJTMC, DRB, EH, LLB, and MJHvO: writing—review and editing.

Conflict of interest

The authors declare no conflict of interest.

Funding

The work was supported by Botany foundation and Early Career Research scheme from the University of Melbourne [grant number 2022ECR088] to PD. PD, SJTMC, DRB, EH, MJHvO, and LLB were supported by the Gordon & Betty Moore Foundation [grant number 9351]. MJHvO and MRN were supported by an Australian Research Council Laureate Fellowship and Marsden Fast Start from the Royal Society Te Apārangi [grant numbers FL180100036 and MFP-VUW2103], respectively.

Data availability

The numeric data that support the findings of this study are openly available at the Figshare repository https://doi.org/10.6084/m9.figshare.25511563.v1 (Deore *et al.*, 2024), and ITS2 profiles of the strains are available on SymPotal.org.

References

Aihara Y, Takahashi S, Minagawa J. 2016. Heat induction of cyclic electron flow around photosystem I in the symbiotic dinoflagellate *Symbiodinium*. Plant Physiology **171**, 522–529.

Allorent G, Tokutsu R, Roach T, *et al*. 2013. A dual strategy to cope with high light in *Chlamydomonas reinhardtii*. The Plant Cell **25**, 545–557.

Asada K. 2019. Production and action of active oxygen species in photosynthetic tissues. In: Foyer C, Mullineaux P, eds. Causes of photooxidative stress and amelioration of defense systems in plants. New York: CRC Press, 77–104.

Baker AC. 2003. Flexibility and specificity in coral-algal symbiosis: diversity, ecology, and biogeography of *Symbiodinium*. Annual Review of Ecology, Evolution, and Systematics **34**, 661–689.

Baker AC. 2004. Symbiont diversity on coral reefs and its relationship to bleaching resistance and resilience. In: Rosenberg E, Loya Y, eds. Coral health and disease. Berlin, Heidelberg: Springer, 177–194.

Baum JK, Claar DC, Tietjen KL, Magel JMT, Maucieri DG, Cobb KM, McDevitt-Irwin JM. 2023. Transformation of coral communities subjected to an unprecedented heatwave is modulated by local disturbance. Science Advances **9**, eabq5615.

Bayliss SL, Scott ZR, Coffroth MA, terHorst CP. 2019. Genetic variation in *Breviolum antillogorgium*, a coral reef symbiont, in response to temperature and nutrients. Ecology and Evolution **9**, 2803–2813.

Berkelmans R, van Oppen MJ. 2006. The role of zooxanthellae in the thermal tolerance of corals: a 'nugget of hope' for coral reefs in an era of climate change. Proceedings of the Royal Society B: Biological Sciences **273**, 2305–2312.

Bojko M, Olchawa-Pajor M, Goss R, Schaller-Laudel S, Strzałka K, Latowski D. 2019. Diadinoxanthin de-epoxidation as important factor in the short-term stabilization of diatom photosynthetic membranes exposed to different temperatures. Plant, Cell & Environment **42**, 1270–1286.

Bonente G, Ballottari M, Truong TB, Morosinotto T, Ahn TK, Fleming GR, Niyogi KK, Bassi R. 2011. Analysis of LhcSR3, a protein essential for feedback de-excitation in the green alga *Chlamydomonas reinhardtii*. PLoS Biology **9**, e1000577.

Buerger P, Alvarez-Roa C, Coppin C, Pearce S, Chakravarti L, Oakeshott J, Edwards O, van Oppen M. 2020. Heat-evolved microalgal symbionts increase coral bleaching tolerance. Science Advances **6**, eaba2498.

Chemeris YK, Shenderova L, Venediktov P, Rubin A. 2004. Activation of chlororespiration increases chlorophyll fluorescence yield in *Chlorella* adapted to darkness at high temperature. Biology Bulletin of the Russian Academy of Sciences **31**, 143–150.

Christa G, Cruz S, Jahns P, de Vries J, Cartaxana P, Esteves AC, Serôdio J, Gould SB. 2017. Photoprotection in a monophyletic branch of chlorophyte algae is independent of energy-dependent quenching (qE). New Phytologist **214**, 1132–1144.

Coles SL, Jokiel PL. 1978. Synergistic effects of temperature, salinity and light on the hermatypic coral *Montipora verrucosa*. Marine Biology **49**, 187–195.

Cunning R, Gillette P, Capo T, Galvez K, Baker AC. 2015. Growth tradeoffs associated with thermotolerant symbionts in the coral *Pocillopora damicornis* are lost in warmer oceans. Coral Reefs **34**, 155–160.

Dang KV, Pierangelini M, Roberty S, Cardol P. 2019. Alternative photosynthetic electron transfers and bleaching phenotypes upon acute heat stress in *Symbiodinium* and *Breviolum* spp. (Symbiodiniaceae) in culture. Frontiers in Marine Science **6**, 656.

Davies SW, Gamache MH, Howe-Kerr LI, *et al*. 2023. Building consensus around the assessment and interpretation of Symbiodiniaceae diversity. PeerJ **11**, e15023.

Deore P, Tsang Min Ching SJ, Nitschke MR, Rudd D, Brumley DR, Hinde E, Blackall LL, van Oppen MJ. 2024. Data from: Unique photosynthetic strategies employed by closely related *Breviolum minutum* strains under rapid short-term cumulative heat stress. Figshare, https://doi.org/10.6084/m9.figshare.25511563.v1

Díaz-Almeyda E, Thomé P, El Hafidi M, Iglesias-Prieto R. 2011. Differential stability of photosynthetic membranes and fatty acid composition at elevated temperature in *Symbiodinium*. Coral Reefs **30**, 217–225.

Díaz-Almeyda EM, Prada C, Ohdera A, Moran H, Civitello D, Iglesias-Prieto R, Carlo T, LaJeunesse T, Medina M. 2017. Intraspecific and interspecific variation in thermotolerance and photoacclimation in *Symbiodinium* dinoflagellates. Proceedings of the Royal Society B: Biological Sciences **284**, 20171767.

Dilernia NJ, Camp EF, Bartels N, Suggett DJ. 2023. Contrasting the thermal performance of cultured coral endosymbiont photo-physiology. Journal of Experimental Marine Biology and Ecology **561**, 151865.

Dubinsky Z, Jokiel PL. 1994. Ratio of energy and nutrient fluxes regulates symbiosis between zooxanthellae and corals. The Biological Bulletin **141**, 350–363.

Dungan AM, Hartman LM, Blackall LL, van Oppen MJ. 2022. Exploring microbiome engineering as a strategy for improved thermal tolerance in *Exaiptasia diaphana*. Journal of Applied Microbiology **132**, 2940–2956.

Dungan AM, Hartman LM, Tortorelli G, Belderok R, Lamb AM, Pisan L, McFadden GI, Blackall LL, van Oppen MJ. 2020. *Exaiptasia diaphana* from the great barrier reef: a valuable resource for coral symbiosis research. Symbiosis **80**, 195–206.

Eilers P, Peeters J. 1988. A model for the relationship between light intensity and the rate of photosynthesis in phytoplankton. Ecological Modelling **42**, 199–215.

Ezequiel J, Nitschke MR, Laviale M, Serôdio J, Frommlet JC. 2023. Concurrent bioimaging of microalgal photophysiology and oxidative stress. Photosynthesis Research **155**, 177–190.

Figueroa R, Howe-Kerr L, Correa A. 2021. Direct evidence of sex and a hypothesis about meiosis in Symbiodiniaceae. Scientific Reports **11**, 18838.

Goss R, Lepetit B. 2015. Biodiversity of NPQ. Journal of Plant Physiology **172**, 13–32.

Herdean A, Hall C, Hughes DJ, Kuzhiumparambil U, Diocaretz BC, Ralph PJ. 2023. Temperature mapping of non-photochemical quenching in *Chlorella vulgaris*. Photosynthesis Research **155**, 191–202.

Hill R, Larkum A, Prášil O, Kramer D, Szabó M, Kumar V, Ralph P. 2012. Light-induced dissociation of antenna complexes in the symbionts of scleractinian corals correlates with sensitivity to coral bleaching. Coral Reefs **31**, 963–975.

Hoadley KD, Pettay DT, Lewis A, Wham D, Grasso C, Smith R, Kemp DW, LaJeunesse T, Warner ME. 2021. Different functional traits among closely related algal symbionts dictate stress endurance for vital Indo-Pacific reef-building corals. Global Change Biology **27**, 5295–5309.

Hoegh-Guldberg O. 1999. Climate change, coral bleaching and the future of the world's coral reefs. Marine and Freshwater Research **50**, 839–866.

Howells E, Beltran V, Larsen N, Bay L, Willis B, Van Oppen M. 2012. Coral thermal tolerance shaped by local adaptation of photosymbionts. Nature Climate Change **2**, 116–120.

Hume B, D'angelo C, Burt J, Baker A, Riegl B, Wiedenmann J. 2013. Corals from the Persian/Arabian Gulf as models for thermotolerant reef-builders: prevalence of clade C3 *Symbiodinium*, host fluorescence and ex situ temperature tolerance. Marine Pollution Bulletin **72**, 313–322.

Hume BC, D'Angelo C, Smith EG, Stevens JR, Burt J, Wiedenmann J. 2015. *Symbiodinium thermophilum* sp. nov., a thermotolerant symbiotic alga prevalent in corals of the world's hottest sea, the Persian/Arabian Gulf. Scientific Reports **5**, 8562.

Hume BC, Smith EG, Ziegler M, Warrington HJ, Burt JA, LaJeunesse TC, Wiedenmann J, Voolstra CR. 2019. SymPortal: a novel analytical framework and platform for coral algal symbiont next-generation sequencing ITS2 profiling. Molecular Ecology Resources **19**, 1063–1080.

Ilík P, Špundová M, Šicner M, *et al*. 2018. Estimating heat tolerance of plants by ion leakage: a new method based on gradual heating. New Phytologist **218**, 1278–1287.

Johnson X, Steinbeck J, Dent RM, *et al*. 2014. Proton gradient regulation 5-mediated cyclic electron flow under ATP- or redox-limited

conditions: a study of Δ*ATPase pgr5* and Δ*rbcL pgr5* mutants in the green alga *Chlamydomonas reinhardtii*. Plant Physiology **165**, 438–452.

Kato H, Tokutsu R, Kubota-Kawai H, Burton-Smith RN, Kim E, Minagawa J. 2020. Characterization of a giant PSI supercomplex in the symbiotic dinoflagellate Symbiodiniaceae. Plant Physiology **183**, 1725–1734.

Kato MC, Hikosaka K, Hirotsu N, Makino A, Hirose T. 2003. The excess light energy that is neither utilized in photosynthesis nor dissipated by photoprotective mechanisms determines the rate of photoinactivation in photosystem II. Plant and Cell Physiology **44**, 318–325.

Kihara S, Hartzler DA, Savikhin S. 2014. Oxygen concentration inside a functioning photosynthetic cell. Biophysical Journal **106**, 1882–1889.

Klughammer C, Schreiber U. 2008. Complementary PS II quantum yields calculated from simple fluorescence parameters measured by PAM fluorometry and the Saturation Pulse method. PAM Application Notes **1**, 201–247.

Kramer DM, Johnson G, Kiirats O, Edwards GE. 2004. New fluorescence parameters for the determination of Q_A redox state and excitation energy fluxes. Photosynthesis Research **79**, 209–218.

Lajeunesse TC, Parkinson JE, Reimer JD. 2012. A genetics-based description of *Symbiodinium minutum* sp. nov. and *S. psygmophilum* sp. nov. (Dinophyceae), two dinoflagellates symbiotic with cnidaria. Journal of Phycology **48**, 1380–1391.

Lepetit B, Volke D, Gilbert M, Wilhelm C, Goss R. 2010. Evidence for the existence of one antenna-associated, lipid-dissolved and two protein-bound pools of diadinoxanthin cycle pigments in diatoms. Plant Physiology **154**, 1905–1920.

Mansour JS, Pollock FJ, Díaz-Almeyda E, Iglesias-Prieto R, Medina M. 2018. Intra-and interspecific variation and phenotypic plasticity in thylakoid membrane properties across two *Symbiodinium* clades. Coral Reefs **37**, 841–850.

Maxwell K, Johnson GN. 2000. Chlorophyll fluorescence—a practical guide. Journal of Experimental Botany **51**, 659–668.

Müller P, Li XP, Niyogi KK. 2001. Non-photochemical quenching. A response to excess light energy. Plant Physiology **125**, 1558–1566.

Murchie EH, Lawson T. 2013. Chlorophyll fluorescence analysis: a guide to good practice and understanding some new applications. Journal of Experimental Botany **64**, 3983–3998.

Neubauer C, Yamamoto HY. 1994. Membrane barriers and Mehler-peroxidase reaction limit the ascorbate available for violaxanthin de-epoxidase activity in intact chloroplasts. Photosynthesis Research **39**, 137–147.

Nielsen DA, Petrou K, Gates RD. 2018. Coral bleaching from a single cell perspective. The ISME Journal **12**, 1558–1567.

Nitschke MR, Rosset SL, Oakley CA, Gardner SG, Camp EF, Suggett DJ, Davy SK. 2022. The diversity and ecology of Symbiodiniaceae: a traits-based review. Advances in Marine Biology **92**, 55–127.

Oxborough K, Baker NR. 1997. Resolving chlorophyll a fluorescence images of photosynthetic efficiency into photochemical and non-photochemical components–calculation of qP and F_v/F_m; without measuring F_o. Photosynthesis Research **54**, 135–142.

Pierangelini M, Thiry M, Cardol P. 2020. Different levels of energetic coupling between photosynthesis and respiration do not determine the occurrence of adaptive responses of Symbiodiniaceae to global warming. New Phytologist **228**, 855–868.

Quaas T, Berteotti S, Ballottari M, Flieger K, Bassi R, Wilhelm C, Goss R. 2015. Non-photochemical quenching and xanthophyll cycle activities in six green algal species suggest mechanistic differences in the process of excess energy dissipation. Journal of Plant Physiology **172**, 92–103.

Ralph PJ, Gademann R. 2005. Rapid light curves: a powerful tool to assess photosynthetic activity. Aquatic Botany **82**, 222–237.

Reynolds JM, Bruns BU, Fitt WK, Schmidt GW. 2008. Enhanced photoprotection pathways in symbiotic dinoflagellates of shallow-water corals and other cnidarians. Proceedings of the National Academy of Sciences, USA **105**, 13674–13678.

Roberty S, Bailleul B, Berne N, Franck F, Cardol P. 2014. PSI Mehler reaction is the main alternative photosynthetic electron pathway in *Symbiodinium* sp., symbiotic dinoflagellates of cnidarians. New Phytologist **204**, 81–91.

Rochaix J-D. 2014. Regulation and dynamics of the light-harvesting system. Annual Review of Plant Biology **65**, 287–309.

Rodrigues JS, Kovács L, Lukeš M, Höper R, Steuer R, Červený J, Lindberg P, Zavřel T. 2023. Characterizing isoprene production in cyanobacteria—Insights into the effects of light, temperature, and isoprene on *Synechocystis* sp. PCC 6803. Bioresource Technology **380**, 129068.

Roháček K, Bertrand M, Moreau B, Jacquette B, Caplat C, Morant-Manceau A, Schoefs B. 2014. Relaxation of the non-photochemical chlorophyll fluorescence quenching in diatoms: kinetics, components and mechanisms. Philosophical Transactions of the Royal Society of London, Series B: Biological Sciences **369**, 20130241.

Ros M. 2020. Adaptive strategies of carbon transformation amongst coral symbionts (Symbiodiniaceae). Sydney, Australia: University of Technology Sydney.

Rowan R, Knowlton N. 1995. Intraspecific diversity and ecological zonation in coral-algal symbiosis. Proceedings of the National Academy of Sciences, USA **92**, 2850–2853.

Russnak V, Rodriguez-Lanetty M, Karsten U. 2021. Photophysiological tolerance and thermal plasticity of genetically different Symbiodiniaceae endosymbiont species of *Cnidaria*. Frontiers in Marine Science **323**, 657348.

Scharfenstein HJ, Alvarez-Roa C, Peplow LM, Buerger P, Chan WY, van Oppen MJ. 2023. Chemical mutagenesis and thermal selection of coral photosymbionts induce adaptation to heat stress with trait trade-offs. Evolutionary Applications **16**, 1549–1567.

Schreiber U. 2004. Pulse-Amplitude-Modulation (PAM) Fluorometry and saturation pulse method: an overview. In: Papageorgiou GC, Govindjee, eds. Chlorophyll *a* fluorescence: a signature of photosynthesis. Dordrecht: Springer Netherlands, 279–319.

Schreiber U, Klughammer C. 2008. Non-photochemical fluorescence quenching and quantum yields in PS I and PS II: analysis of heat-induced limitations using Maxi-Imaging-PAM and Dual-PAM-100. PAM Application Notes **1**, 15–18.

Serôdio J, Ezequiel J, Frommlet J, Laviale M, Lavaud J. 2013. A method for the rapid generation of nonsequential light-response curves of chlorophyll fluorescence. Plant Physiology **163**, 1089–1102.

Silverstein RN, Cunning R, Baker AC. 2015. Change in algal symbiont communities after bleaching, not prior heat exposure, increases heat tolerance of reef corals. Global Change Biology **21**, 236–249.

Sinutok S, Chotikarn P, Saengsakda Pattaratumrong M, Moungkeaw P, Pramneechote P, Yucharoen M. 2022. Synergistic effect of elevated temperature and light stresses on physiology of *Pocillopora acuta* from different environments. Journal of Marine Science and Engineering **10**, 790.

Slavov C, Schrameyer V, Reus M, Ralph PJ, Hill R, Büchel C, Larkum AW, Holzwarth AR. 2016. 'Super-quenching' state protects *Symbiodinium* from thermal stress—implications for coral bleaching. Biochimica Et Biophysica Acta (BBA) –Bioenergetics **1857**, 840–847.

Sommella E, Conte GM, Salviati E, Pepe G, Bertamino A, Ostacolo C, Sansone F, Prete FD, Aquino RP, Campiglia P. 2018. Fast profiling of natural pigments in different spirulina (*Arthrospira platensis*) dietary supplements by DI-FT-ICR and evaluation of their antioxidant potential by pre-column DPPH-UHPLC assay. Molecules **23**, 1152.

Starko S, Fifer JE, Claar DC, Davies SW, Cunning R, Baker AC, Baum JK. 2023. Marine heatwaves threaten cryptic coral diversity and erode associations among coevolving partners. Science Advances **9**, eadf0954.

Tchernov D, Gorbunov MY, de Vargas C, Narayan Yadav S, Milligan AJ, Häggblom M, Falkowski PG. 2004. Membrane lipids of symbiotic algae are diagnostic of sensitivity to thermal bleaching in corals. Proceedings of the National Academy of Sciences, USA **101**, 13531–13535.

Tortorelli G, Belderok R, Davy SK, McFadden GI, van Oppen MJ. 2020. Host genotypic effect on algal symbiosis establishment in the coral

model, the anemone *Exaiptasia diaphana*, from the Great Barrier Reef. Frontiers in Marine Science **6**, 833.

Travesso M, Missionário M, Cruz S, Calado R, Madeira D. 2023. Combined effect of marine heatwaves and light intensity on the cellular stress response and photophysiology of the leather coral *Sarcophyton* cf. *glaucum*. The Science of the Total Environment **861**, 160460.

van Oppen MJ, Baker AC, Coffroth MA, Willis BL. 2009. Bleaching resistance and the role of algal endosymbionts. In: van Oppen MJ, Lough JM, eds. Coral bleaching: patterns, processes, causes and consequences. Berlin, Heidelberg: Springer, 83–102.

Venn AA, Wilson MA, Trapido-Rosenthal HG, Keely BJ, Douglas AE. 2006. The impact of coral bleaching on the pigment profile of the symbiotic alga, *Symbiodinium*. Plant, Cell & Environment **29**, 2133–2142.

Wang W, Zhang X, Garcia S, Leitch AR, Kovařík A. 2023. Intragenomic rDNA variation-the product of concerted evolution, mutation, or something in between? Heredity **131**, 179–188.

Weis VM. 2008. Cellular mechanisms of Cnidarian bleaching: stress causes the collapse of symbiosis. The Journal of Experimental Biology **211**, 3059–3066.

Wilk L, Grunwald M, Liao P-N, Walla PJ, Kühlbrandt W. 2013. Direct interaction of the major light-harvesting complex II and PsbS in nonphotochemical quenching. Proceedings of the National Academy of Sciences, USA **110**, 5452–5456.

Wilson K, Li Y, Whan V, *et al*. 2002. Genetic mapping of the black tiger shrimp *Penaeus monodon* with amplified fragment length polymorphism. Aquaculture **204**, 297–309.

Xiao L, Johansson S, Rughöft S, Burki F, Sandin MM, Tenje M, Behrendt L. 2022. Photophysiological response of Symbiodiniaceae single cells to temperature stress. The ISME Journal **16**, 2060–2064.

Zaks J, Amarnath K, Kramer DM, Niyogi KK, Fleming GR. 2012. A kinetic model of rapidly reversible nonphotochemical quenching. Proceedings of the National Academy of Sciences, USA **109**, 15757–15762.